The Cryosphere

Sea-ice deformation in a coupled ocean–sea-ice model and in satellite remote sensing data

Gunnar Spreen[1,2], **Ron Kwok**[2], **Dimitris Menemenlis**[2], **and An T. Nguyen**[2,a]

[1]University of Bremen, Institute of Environmental Physics, Bremen, Germany
[2]Jet Propulsion Laboratory, California Institute of Technology, Pasadena, CA, USA
[a]now at: The University of Texas at Austin, Austin, TX, USA

Correspondence to: Gunnar Spreen (gunnar.spreen@uni-bremen.de)

Abstract. A realistic representation of sea-ice deformation in models is important for accurate simulation of the sea-ice mass balance. Simulated sea-ice deformation from numerical simulations with 4.5, 9, and 18 km horizontal grid spacing and a viscous–plastic (VP) sea-ice rheology are compared with synthetic aperture radar (SAR) satellite observations (RGPS, RADARSAT Geophysical Processor System) for the time period 1996–2008. All three simulations can reproduce the large-scale ice deformation patterns, but small-scale sea-ice deformations and linear kinematic features (LKFs) are not adequately reproduced. The mean sea-ice total deformation rate is about 40 % lower in all model solutions than in the satellite observations, especially in the seasonal sea-ice zone. A decrease in model grid spacing, however, produces a higher density and more localized ice deformation features. The 4.5 km simulation produces some linear kinematic features, but not with the right frequency. The dependence on length scale and probability density functions (PDFs) of absolute divergence and shear for all three model solutions show a power-law scaling behavior similar to RGPS observations, contrary to what was found in some previous studies. Overall, the 4.5 km simulation produces the most realistic divergence, vorticity, and shear when compared with RGPS data. This study provides an evaluation of high and coarse-resolution viscous–plastic sea-ice simulations based on spatial distribution, time series, and power-law scaling metrics.

1 Introduction

The Arctic sea ice in many respects is an important component of the Earth's climate system, e.g., sea ice governs the ocean-to-atmosphere heat flux, freezing and melting influences the upper ocean salinity and density, and sea-ice dynamics act as a latent energy transport (Barry et al., 1993). During recent years substantial changes of the Arctic sea-ice cover have been observed (e.g., Comiso et al., 2008; Kwok and Rothrock, 2009; Nghiem et al., 2007). Coupled ocean–sea-ice models can reproduce some aspects of sea ice and its recent changes (e.g., Zhang et al., 2008; Lindsay et al., 2009; Nguyen et al., 2011). In part this can be attributed to the fact that model parameters can be adjusted to produce observed ice concentration (extent) and drift distributions (Nguyen et al., 2011; Fenty et al., 2015). Detailed comparisons between satellite remote sensing data with model results, however, reveal big differences in certain aspects of the sea-ice cover, e.g., for fracture zones and for small-scale dynamic processes (Kwok et al., 2008; Girard et al., 2009). It remains unclear whether current model physics are suited to reproduce these observed sea-ice deformation features (Coon et al., 2007) or if new sea-ice rheologies (e.g., Bouillon and Rampal, 2015b; Girard et al., 2011; Sulsky et al., 2007) have to be used. Sea-ice deformation is an important process for (1) sea-ice mass balance due to new ice production and ridged ice formation, (2) brine rejection into the ocean due to freezing in open water areas, (3) regulation of ocean-to-air heat and gas fluxes, and (4) altering the air and water drag coefficients. Therefore a realistic representation of sea-ice deformation in coupled sea-ice–ocean models is important.

Here we study sea-ice deformation strain rates in the Arctic obtained from synthetic aperture radar (SAR) satellite measurements using the RADARSAT Geophysical Processor System (RGPS) in comparison to coupled ocean–sea-ice simulations carried out with the Massachusetts Institute of Technology general circulation model (MITgcm) as configured for the Estimating the Circulation and Climate of the Ocean, Phase II (ECCO2) project (Menemenlis et al., 2008). Model integrations with horizontal grid spacing of 18, 9, and 4.5 km are carried out. These comparisons also allow us to study the model uncertainties regarding the sea-ice deformation representation in the current formulation of viscous–plastic (VP) sea-ice models.

Traditionally sea-ice model performance is evaluated by comparing satellite-derived ice area and velocities to model results (e.g., Nguyen et al., 2011; Zhang et al., 2003). However, it can be shown that the Arctic sea-ice velocity field can be divided into mean and fluctuating fields, with the fluctuating field not behaving in a significantly different manner from a turbulent fluid (Rampal et al., 2009). It is therefore not sufficient to evaluate models on the basis of their first-order mean velocity field. Kwok et al. (2008) showed that sea-ice models that reproduce the large-scale ice velocity field can still have large problems in reproducing sea-ice deformations correctly. The second-order sea-ice velocity field, represented by the sea-ice deformation fields (strain rate invariants) has to be used for comparison to take into account the high-frequency fluctuations of the sea-ice velocity field and to assess the quality of the sea-ice rheology formulation.

Sea-ice strain rates do not scale linearly in space and time but follow a power law depending on the length scale L and time interval ΔT over which the strain rates are integrated. For RGPS total deformation rates $\dot{D}$ in the Arctic, Marsan et al. (2004) and Stern and Lindsay (2009) observe a spatial-scale dependence of $\dot{D} \approx dL^{-0.2}$ over a scale range from 10 to 1000 km. The constant d can be interpreted as the mean deformation rate at a given base scale. To make meaningful comparisons between observations and model simulations, both have to be brought to the same reference frame in space and time, i.e., averages have to be calculated for the same area and time interval. Otherwise the scaling nonlinearity will cause artificial differences between the datasets.

It can be shown that traditional sea-ice models using the Hibler (1979) viscous–plastic or elastic–viscous–plastic (EVP) (Hunke and Dukowicz, 1997) ice rheology have difficulties in correctly representing the sea-ice deformation fields, especially the distribution of the observed linear kinematic features (LKFs) (Kwok et al., 2008; Lindsay et al., 2003; Wang and Wang, 2009). Girard et al. (2009) also report distinct differences in the statistical scaling behavior of RGPS data and models using VP and EVP sea-ice rheologies, showing that the modeled deformation distributions can be close to Gaussian while the observed ones follow a power law. Improvements in modeled sea-ice deformation and thickness can be obtained by modifying the form of the yield curve away from an elliptical shape and/or changing the ratio of major to minor axes (Wang and Wang, 2009; Miller et al., 2005). To overcome some of the deficiencies of the viscous–plastic rheology, new ice rheologies with improved ice physics are under development in the hope of better representing the observed sea-ice dynamics (e.g., Heil and Hibler, 2002; Sulsky et al., 2007; Girard et al., 2011; Bouillon and Rampal, 2015b). A recent example is the study of Tsamados et al. (2013), which demonstrates how an anisotropic ice rheology changes the sea-ice mass balance and ice dynamics compared to the EVP rheology. Current VP and EVP sea-ice model implementations, however, are robust and their parameters well tuned to reproduce the broad features of sea-ice extent and drift. Therefore, they are widely used in coupled ocean–sea ice and in global climate simulations, and thus their evaluation is necessary.

The main purpose of this article is to examine how model grid spacing influences simulated sea-ice deformation representation when compared to satellite observations. Different from previous studies, we focus on direct comparison between the modeled and observed strain rates. Using the VP model, we construct simulated deformation fields on the same spatial and temporal scales as in the RGPS observations (Sect. 2.3) and compare them spatially (Sect. 3.1). We then analyze the power-law scaling properties of the modeled and observed deformation rates (Sect. 3.2). Ultimately, we would like to highlight why the sea-ice strength representation and the sea-ice rheology should receive more attention in models.

The remainder of this article is laid out as follows: Sect. 2 describes the model setup and introduces the RGPS satellite data. Section 3 contains the comparison between modeled sea-ice deformation and RGPS satellite observations. It contains an evaluation of the representation of sea-ice deformation dependencies on horizontal grid spacing, both spatially and as time series, and shows the power-law scaling behavior of the modeled and observed sea-ice deformation fields. Finally, Sect. 4 concludes and further discusses the results.

2 Model setup and satellite data

2.1 MITgcm Arctic model setup

The model output used for this study is obtained from integrations of a coupled ocean and sea-ice configuration of the Massachusetts Institute of Technology general circulation model (MITgcm) (e.g., Losch et al., 2010). The model configuration is similar to that used for global integrations by the Estimating the Circulation and Climate of the Ocean, Phase II project (Menemenlis et al., 2008), but only a subdomain covering the Arctic Ocean including the surrounding marginal seas and parts of the North Atlantic and Pacific is used (see Fig. 1a).

Briefly, the ECCO2 project uses a cube sphere grid projection in a volume-conserving C-grid configuration. The ocean
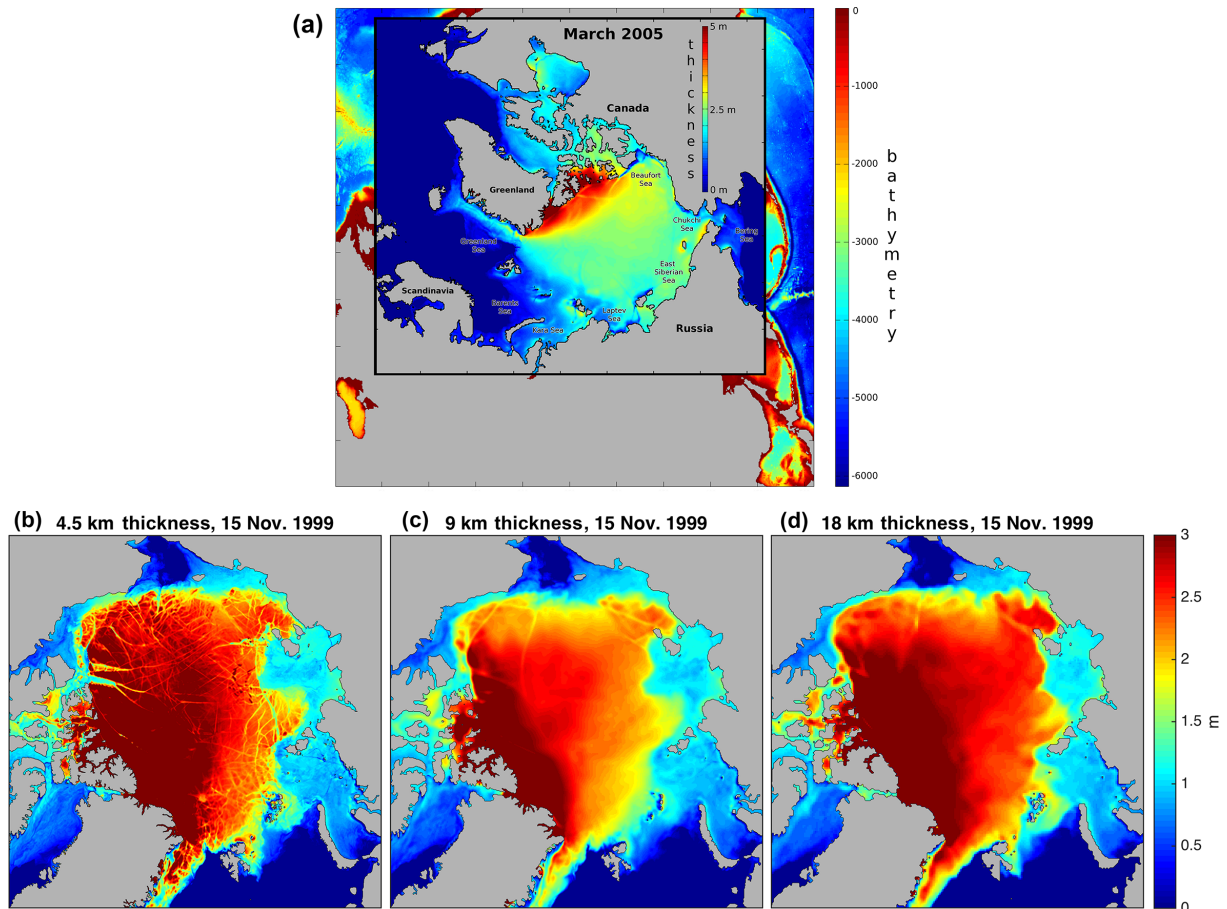
Figure 1. (a) The Arctic face of the cube sphere grid used by the ECCO2 project. The March 2005 ice thickness inset shows the regional grid used in this study. Note that the North Pacific coastline in the regional grid is modified relative to the global setup in order to remove unconnected seas. Boundary conditions are obtained from the ECCO2 18 km cube sphere solution. **(b–d)** Sea-ice thickness on 15 November 1999 after about 8 years of model integration for the 4.5, 9, and 18 km simulations, respectively. Sea-ice thickness is shown on the respective original model grid.

model has 50 vertical levels and employs the K-profile parameterization of Large et al. (1994) for vertical mixing. The cold halocline layer of the Arctic Ocean is realistically reproduced with the use of the subgrid-scale brine rejection parameterization of Nguyen et al. (2009). The sea-ice model uses two-category, zero-layer thermodynamics (Hibler, 1980) and viscous–plastic dynamics (Zhang and Hibler III, 1997; Hibler, 1979). The snow cover is simulated following Zhang et al. (1998). Table 1 summarizes the relevant sea-ice parameters used for all model solutions presented herein (see also Nguyen et al., 2011 for more details).

The International Bathymetric Chart of the Arctic Ocean (IBCAO) (Jakobsson et al., 2008) is used as bathymetry, where available. For the remaining part of the model domain, which is not covered by IBCAO, the merged Smith and Sandwell General Bathymetric Charts of the Oceans (GEBCO) is used and blended with IBCAO along the borders. Sea-ice initial conditions (area and thickness) for January 1992 are from the Polar Science Center (Zhang and

Rothrock, 2003), and ocean initial conditions (temperature, salinity, velocity) are from the World Ocean Atlas 2005 (Locarnini et al., 2006; Antonov et al., 2006). The model simulations are started from these initial conditions on 1 January 1992 and end on 31 December 2009. The globally optimized simulation from ECCO2 (Menemenlis et al., 2008) provides lateral boundary conditions. Surface boundary conditions are obtained from the Japanese 25-year Reanalysis (JRA-25; Onogi et al., 2007) with a spatial and temporal resolution of 1.125° ($\approx$ 120 km) and 6 h, respectively. These spatial and temporal resolutions do not allow to fully resolve all high-frequency atmospheric forcing on the sea ice. Some ice deformation events will be missed, which adds uncertainty to model-derived sea-ice deformation rates.

Integrations with three different nominal horizontal grid spacings, 18, 9, and 4.5 km, were performed. An example of the simulated sea-ice thickness on 15 November 1999, after about 8 years of model integration, is shown in Fig. 1b–d for the three different grid spacings. The 4.5 km solutions

Table 1. Selected sea-ice model parameters (see Nguyen et al., 2011, for more details).

Atmospheric forcing	JRA-25	
Sea-ice dry albedo	0.7	
Sea-ice wet albedo	0.71	
Snow dry albedo	0.87	
Snow wet albedo	0.81	
Ocean albedo	0.16	
Air–sea-ice drag coefficient	0.0011	
Ocean–sea-ice drag coefficient	0.0054	
Ice strength parameter P^*	23	$kN\,m^{-2}$
Lead closing parameter H_o	0.6	
Elliptical yield curve major to minor axis ratio e	2	

Table 2. RGPS periods used in this study. Column 3 gives the number of monthly mean values used.

Start date	End date	No./months	Season
1996-11-07	1997-06-01	7	winter
1997-05-18	1997-08-01	2	summer
1997-11-02	1998-06-01	7	winter
1998-05-10	1998-09-01	2	summer
1998-10-28	1999-05-17	6	winter
1999-05-08	1999-09-01	4	summer
1999-11-01	2000-05-14	7	winter
2000-11-04	2001-06-01	7	winter
2001-05-15	2001-09-01	3	summer
2001-11-05	2002-06-01	7	winter
2002-05-16	2002-08-01	2	summer
2003-12-04	2004-06-01	6	winter
2004-05-11	2004-09-01	3	summer
2004-11-10	2005-06-01	7	winter
2005-05-15	2005-09-01	3	summer
2005-11-29	2006-06-01	6	winter
2006-05-19	2006-09-01	3	summer
2006-12-03	2007-06-01	6	winter
2007-05-14	2007-09-01	3	summer
2007-12-01	2008-06-01	6	winter
20 periods (11 winter/9 summer)		97	

clearly show more details, e.g., clearer lead patterns, that is, regions with reduced ice thickness. Since typical lead width is smaller than the model grid spacing, the ice thickness does not drop to zero. The 18 km model solution was constrained by least squares fit to available satellite and in situ data (e.g., ice drift, area, thickness) using a Green's function approach (Menemenlis et al., 2005; Nguyen et al., 2011) and is here referred to as the "baseline" simulation. A comprehensive evaluation of the 18 km model simulation and more detailed description of the optimization can be found in Nguyen et al. (2011). They show, by comparison to measurements, that the model using the optimized parameter set can realistically reproduce the most important features of the coupled Arctic Ocean and sea-ice system. For example, sea-ice extent and thickness as well as their trends are in good agreement with satellite and in situ measurements. Additionally, the sea-ice export through Fram Strait is modeled realistically compared to observations from Kwok et al. (2004). For the higher-resolution (9 and 4.5 km grid spacing) simulations, we use the same set of parameters as those derived for the 18 km configuration. As a consequence these higher-resolution simulations exhibit somewhat larger model deviations relative to observations than the 18 km simulation. For example, the mean ice thickness on 15 November 1999 shown in Fig. 1b–d is similar for the 4.5 and 18 km simulations but higher by 24 and 28 cm, respectively, compared to the 9 km simulation. They nevertheless have been found of sufficient quality for process studies in the Arctic Ocean and adjacent seas (Nguyen et al., 2012; Rignot et al., 2012).

2.2 RGPS satellite observations

The RADARSAT Geophysical Processor System (RGPS) produces sea-ice data products covering the Arctic Ocean derived from synthetic aperture radar imagery acquired by the Canadian RADARSAT satellite. Details of the analysis procedures can be found in the papers of Kwok (1998) and Kwok and Cunningham (2002). In this study the "Lagrangian ice motion" dataset, one of the eight RGPS data products, is

used as initial dataset. Sea-ice deformation, i.e., strain rates, are calculated from this ice motion dataset as described below. We start with the Lagrangian ice motion dataset to allow highest possible consistency between the observed and modeled deformation rates.

The 460 km wide swath ScanSAR Wide B mode of RADARSAT (Raney et al., 1991) is selected to provide routine coverage of the Arctic Ocean for the RGPS system. The western Arctic Ocean is covered by RADARSAT images approximately once every 3 days. At the beginning of the season (winter or summer) an initial Lagrangian grid with 10 km grid spacing is set up. For the start and end dates of winter and summer periods see Table 2. The movement and deformation of the Lagrangian grid cells are followed throughout the season. Grid cells are removed if they are advected out of the region of interest. Gaps in the ice motion datasets are due to the lack of backscatter contrast for tracking ice features in the SAR imagery. The actual sea-ice tracking is very accurate. Lindsay and Stern (2003) report that the median magnitude of displacement differences between buoy drift (via ARGOS positioning) and RGPS motion estimates is 323 m.

RGPS observations are available since November 1996 until May 2008. In this study we use RGPS data from 20 periods (11 winter and 9 summer), or 97 months between 1996 and 2008 (see Table 2).

2.3 Common reference frame for model solutions and observations

As a prerequisite for a meaningful comparison, the Lagrangian RGPS observations and Eulerian model output have to be brought to a common reference frame. We use the RGPS Lagrangian reference frame. This ensures that both RGPS and model sea-ice strain rates are calculated for the same area and time interval. This procedure avoids differences between the datasets caused by the nonlinearity of the strain rate scaling (power-law dependence, see Sects. 1, 3.2, and 3.2.2). The starting point is the RGPS ice drift velocity dataset. After the RGPS and model velocities are brought onto the same reference frame, strain rates are calculated from both datasets in exactly the same way.

Every RGPS Lagrangian point $k(x_i, t_i)$ has a location, time, and time difference Δt until the next observation attached to it. From this $\Delta t = t_{i+1} - t_i$ and the new position x_{i+1}, the velocity of point k during the time interval Δt can be calculated. We interpolate the Eulerian model velocities to the Lagrangian RGPS positions using a bilinear interpolation. The mean RGPS time interval Δt is about 3 days, but Δt varies from a few hours to about 2 weeks. We interpolate the mean model sea-ice velocity during the individual Δt's from the daily model output covering the Δt time period.

After this consistent RGPS and model sea-ice velocity dataset is established, sea-ice strain rates are calculated using Delaunay triangulation. From the triangle area A and the sea-ice velocity components u in x direction and v in y direction at the three triangle corners, the following partial derivatives can be calculated using the Divergence theorem and the line integral around the triangle boundary:

$$\frac{\partial u}{\partial x} = \frac{1}{A} \oint u \mathrm{d}y, \qquad \frac{\partial u}{\partial y} = -\frac{1}{A} \oint u \mathrm{d}x,$$
$$\frac{\partial v}{\partial x} = \frac{1}{A} \oint v \mathrm{d}y, \qquad \frac{\partial v}{\partial y} = -\frac{1}{A} \oint v \mathrm{d}x. \qquad (1)$$

Using Eqs. (1) the strain rate invariants divergence $\dot{\nabla}$, shear $\dot{\tau}$, and vorticity $\dot{\zeta}$ can be calculated:

$$\dot{\nabla} = \frac{\partial u}{\partial x} + \frac{\partial v}{\partial y}, \qquad (2)$$

$$\dot{\tau} = \sqrt{\left(\frac{\partial u}{\partial x} - \frac{\partial v}{\partial y}\right)^2 + \left(\frac{\partial u}{\partial y} + \frac{\partial v}{\partial x}\right)^2}, \qquad (3)$$

$$\dot{\zeta} = \frac{\partial v}{\partial x} - \frac{\partial u}{\partial y}. \qquad (4)$$

As a measure of the total sea-ice deformation rate $\dot{D}$ we use

$$\dot{D} = \sqrt{\dot{\nabla}^2 + \dot{\tau}^2}, \qquad (5)$$

which is used as a measure for the overall sea-ice deformation occurring at a certain point in space (e.g., Stern and Lindsay, 2009).

Erroneous cells, which might, for example, arise due to errors in the ice tracking or from badly defined triangles from the Delaunay triangulation, are filtered out using the following constrains: (1) the triangle cell area A has to be between 5 and 400 km^2. This condition is further restricted to $25 < A < 100$ km^2. This second condition assures that the length scale of all observations can be considered to be ~ 10 km, which is the initial RGPS grid spacing. This is important as sea-ice strain rates are scale dependent (see Sect. 1). (2) Triangles are not allowed to be overly distorted, i.e., not to be acute. To achieve this condition all angles have to be larger than 10°. (3) The time interval Δt between two observations must be between 12 h and 7 days. (4) Cells with a deformation rate $\dot{D}$ (see Eq. 5) higher than 1 day^{-1} are considered outliers and are removed. Only filter (4) creates a different number of observations for the RGPS and model dataset (because $\dot{D}$ can differ between model and RGPS). However, to keep the number of observations equal in both datasets, filtered data points from one dataset are also removed from the other one.

2.4 Anisotropic smoothing filter

Bouillon and Rampal (2015a) show that artificial noise can be present in sea-ice deformation fields derived from Lagrangian sampling. The simplest example to understand the problem, discussed in more detail in the article, would be a linear shear fault line without any divergence, i.e., two floes of ice move parallel to each other in opposite directions. If we now consider Lagrangian points on both sides of the shear line and the triangles they form, it becomes clear that the area of these triangles will change for a parallel but opposite movement of the two floes: alternating the area of the triangles will increase and decrease. Following Eq. (2) this will lead to an alternating pattern of divergence and convergence while actually there is no divergence at all (no lead is opening or closing). This sampling noise can, however, cause the deformation fields to appear noisy and also will artificially increase the absolute divergence, vorticity, and deformation rate (see Eq. 5). Bouillon and Rampal (2015a) estimate an overestimation of opening and closing by about 60 % for the RGPS dataset.

We apply the anisotropic smoothing filter suggested by Bouillon and Rampal (2015a) to all our Lagrangian RGPS and model datasets. We use the same parameters for the filter as suggested in their study, i.e., a threshold of 0.02 day^{-1} for the deformation rate $\dot{D}$ to identify deformed triangles and a smoothing kernel size of $n = 3$. n gives the number of times the kernel size is grown starting from the initially analyzed triangle, i.e., for $n = 1$ only the three triangles adjacent to the analyzed triangles would be used for the smoother. For $n = 3$ this procedure is repeated two more times. All triangles above the threshold values within that kernel are then averaged to yield the new value for the analyzed triangle. For more details see Bouillon and Rampal (2015a). This anisotropic filter will conserve linear structures typical for

ice deformation in most cases and significantly reduce the artificial noise discussed above. The obtained fields will be more realistic and closer to reality.

This smoothing filter is applied to all partial derivatives in Eq. (1) before any further calculations are performed. In the following all results are based on these smoothed ice deformation fields. As explained above the absolute deformation values therefore will be lower than in studies that use the unfiltered deformation fields. The smoother will also affect the scaling exponents discussed in Sect. 3.2. As reference for other studies we therefore repeated all analysis without the anisotropic smoother and present the results in Sect. S1 of the Supplement. In Sect. 3.3 we compare some examples of the filtered and unfiltered results, which will demonstrate that qualitatively all conclusions presented in this study will hold for both the filtered and unfiltered datasets.

3 Modeled sea-ice deformation compared to RGPS observations

In this section, we compare the simulated sea-ice deformation distribution to satellite observations. Big differences between observed and modeled sea-ice deformation fields have been reported (Lindsay et al., 2003; Kwok et al., 2008; Girard et al., 2009; Wang and Wang, 2009, see also Sect. 1). Kwok et al. (2008) evaluated four common sea-ice models with horizontal grid spacing ranging from 9 to 40 km. None of these models could produce realistic distributions of small-scale deformation features and linear kinematic features, although the large-scale sea-ice deformation pattern was reproduced correctly by some of the models. The model with the smallest grid spacing (9 km) showed the most confined LKFs. It was speculated that if the model grid spacing would be further decreased, the model could eventually produce more realistic details and have a better representation of LKF distribution. Girard et al. (2009) compared the statistics of VP and EVP simulations with 12 km grid spacing to RGPS data and also reported large differences, as did Wang and Wang (2009) and Lindsay and Stern (2003), for different model setups. We reconstruct the RGPS observations from model velocity fields for best inter-comparability (Sect. 2.3) and explore how the LKF representation changes when the model resolution increases (Sect. 3.1). We also compare the power-law scaling between our model simulations and the RGPS data (Sect. 3.2).

3.1 Dependence on model grid spacing

3.1.1 Spatial patterns and LKFs: divergence, vorticity, and shear

Figures 2, 3, and 4 show the monthly November 1999 divergence, vorticity, and shear fields, respectively, obtained from RGPS data and from the three model solutions with 4.5, 9, and 18 km grid spacing. November 1999 is shown as an example. Conclusions drawn in this section are qualitatively valid also for other months. Section S2 shows further examples of all three deformation variables for months December 1999 and March and April 2000 to also provide some information about the seasonality of the deformation fields.

Divergence, vorticity, and shear in Figs. 2, 3, and 4 are not calculated from monthly mean ice velocities but are monthly aggregates of the about 3-daily Lagrangian dataset described in Sect. 2.3. The patterns shown are therefore not representative for a single day but are an aggregate of all patterns that have occurred during 1 month. Reoccurring LKFs might overlap each other. For all maps both the Lagrangian RGPS data and the reconstructed Lagrangian model solutions (see Sect. 2.3) were interpolated to the same polar stereographic grid with 12.5 km grid spacing. This means that all differences visible in the model maps (at least for the 9 and 4.5 km ones) are due to changed behavior of the model physics and can not be attributed to the different model grid spacing alone. The 12.5 km grid spacing are a slight oversampling for the 18 km model output but an undersampling for the 9 and 4.5 km model solutions. Figures 2 to 5 also show a black contour discriminating multiyear ice from first-year sea ice based on QuikSCAT backscatter data.

In general, the large-scale sea-ice deformation patterns are reproduced by the model for all three grid spacings. In November 1999 a pattern of high divergence (Fig. 2) can be observed in the Beaufort Sea and a more convergent situation north of the Chukchi and East Siberian Sea (see Figs. 1 and 2 for locations). This pattern is also present in all three model solutions, but it is much weaker. In the RGPS observations the pattern is broader and covering most of the seasonal sea ice in that region. The high divergence in the Beaufort Sea is accompanied by negative vorticity (Fig. 3), which can be observed in the RGPS data as well as in the three model solutions. Additionally, the positive vorticity pattern north of Ellesmere Island with strong LKFs is reproduced in all three model integrations. The same is true for the positive vorticity pattern in the East Siberian Sea and the negative vorticity north of the Laptev Sea.

The RGPS data show strong sea-ice shear almost everywhere in the marginal sea-ice zone (Fig. 4). This area of high shear is only partly reproduced by all three model solutions. All three model solutions show almost no large-scale shear patterns. In the Beaufort and East Siberian seas, only small areas of high shear are present. From the three deformation variables, divergence, shear, and vorticity, the agreement between the large-scale RGPS and model shear is the worst. The agreement of the vorticity patterns between RGPS and models is the best, which is expected because it is strongly inherited from the atmospheric and ocean forcing. However, the magnitudes of divergence, shear, and vorticity for all three model solutions are much smaller (about 40 % smaller, see next section) than the RGPS ones. These statements are true not only for the November 1999 example shown here but
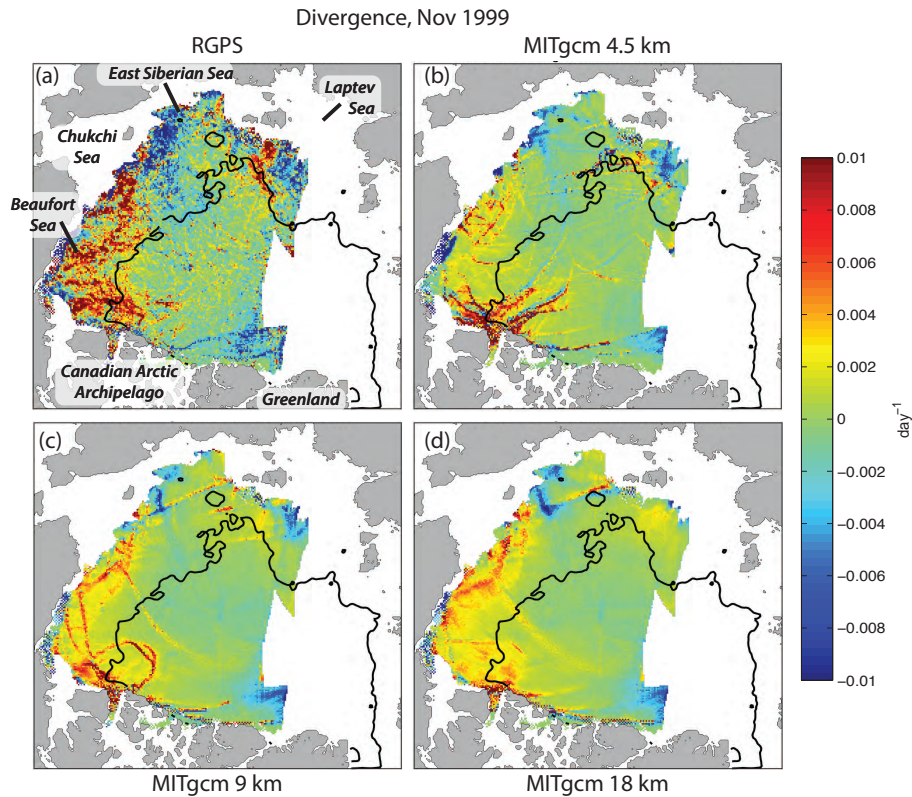
Figure 2. Examples of monthly mean November 1999 sea-ice divergence. The divergence from **(a)** RGPS and the model runs with **(b)** 4.5, **(c)** 9, and **(d)** 18 km grid spacing are shown. The number of LKFs increases with decreasing model grid spacing. All maps are shown on the same 12.5 km grid and are constructed from the same number of observations (see Sect. 2.3). The black line discriminates seasonal and perennial sea ice. White areas are not covered by RGPS observations.

also for almost all of the other months with available RGPS data (see Table 2) and will be further discussed in Sect. 3.1.2.

We now qualitatively compare the distribution and frequency of occurrence of LKFs followed by more quantitative comparisons in the next sections. The model solutions for all three grid spacings do have significantly less LKFs than the RGPS data. This is true for all three deformation variables: divergence, shear, and vorticity. Between the three model solutions there are, however, significant differences for the LKF distribution. While, for example, the sea-ice shear for the 18 km model solution in Fig. 4 shows very few identifiable LKFs, the number of LKFs slightly increases for the 9 km solution and significantly increases for the 4.5 km solution. The same can be observed for the divergence and vorticity fields. The 4.5 km model solution always shows the most LKFs, and its deformation distribution is most consistent with RGPS observations based on visual inspection. This conclusion holds for all 97 months with available RGPS data that were analyzed and will be further discussed in Sect. 3.1.3 (see also Sect. S2 for maps of more example months).

The large-scale difference in sea-ice deformation between RGPS observations and model solutions is not evenly distributed over the Arctic Basin as can already be seen from Figs. 2 to 4. Figure 5 shows the deformation rate difference $\Delta\dot{D} = \dot{D}_{\mathrm{RGPS}} - \dot{D}_{\mathrm{MODEL}}$ for the 4.5, 9, and 18 km solutions during November 1999. All three difference maps are smoothed with a 150 km kernel to remove small-scale differences (e.g., LKFs) and highlight the large-scale difference patterns. The large-scale difference patterns are very similar for all three model grid spacings. The representation of large-scale sea-ice deformation in the model is therefore less dependent on the model grid spacing than the small-scale deformation distribution. There is, however, some seasonal dependence as we will see in Sect. 3.1.2.

The main differences in $\Delta\dot{D}$ are confined to the seasonal ice zone (outside the black contour in Fig. 5). In general the seasonal sea ice is thinner and more mobile than the older, thicker perennial ice. For the perennial ice, $\Delta\dot{D}$ is much smaller and mainly stays below $0.02\,\mathrm{day}^{-1}$. This discrepancy between seasonal and perennial ice hints to a shortcoming of the sea-ice rheology used in the simulations. Foremost, seasonal, and perennial sea ice can be discriminated by their respective thickness. Our November 1999 example month, however, also covers very young ice in the marginal ice zone (MIZ), where also floe size and the level of fragmentation
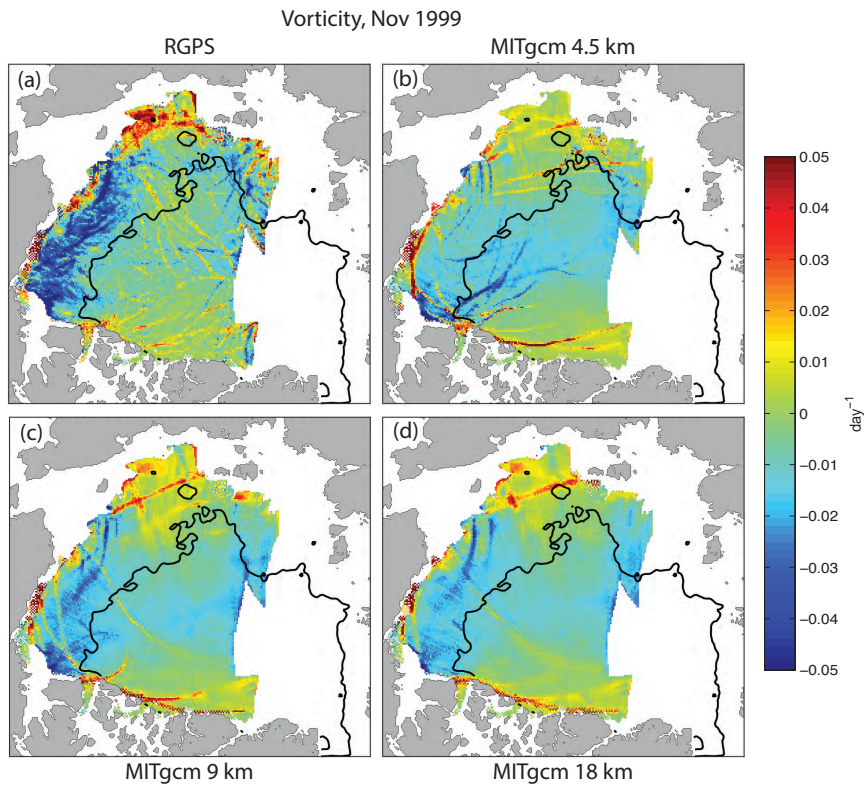
Vorticity, Nov 1999

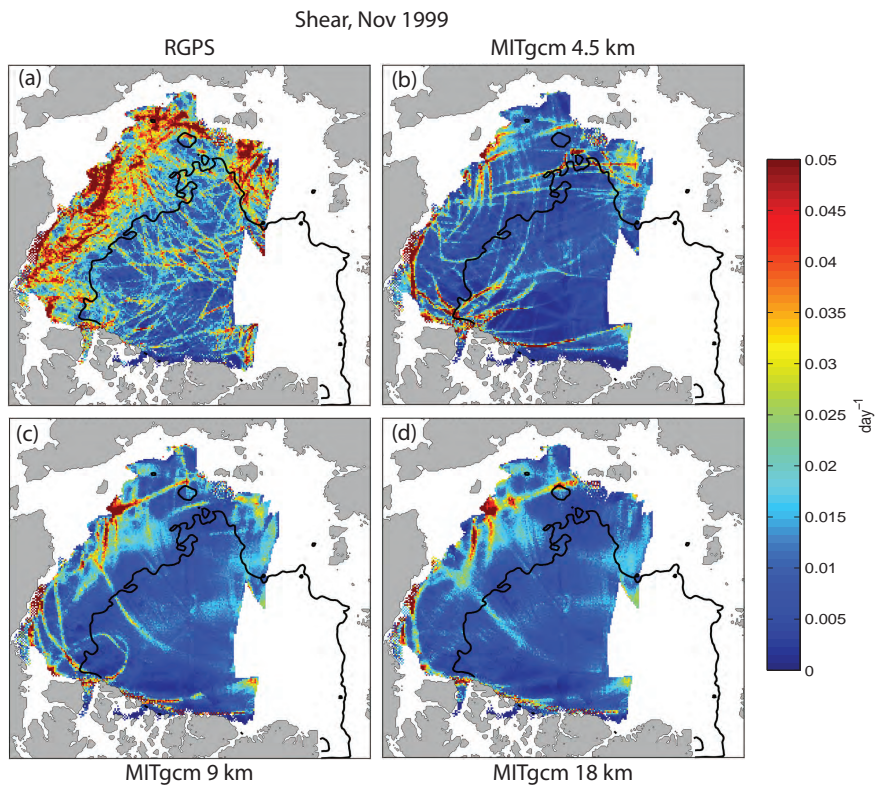**Figure 3.** As Fig. 2 but for vorticity.

Shear, Nov 1999

Figure 4. As Fig. 2 but for shear.

Deformation rate difference, Nov 1999
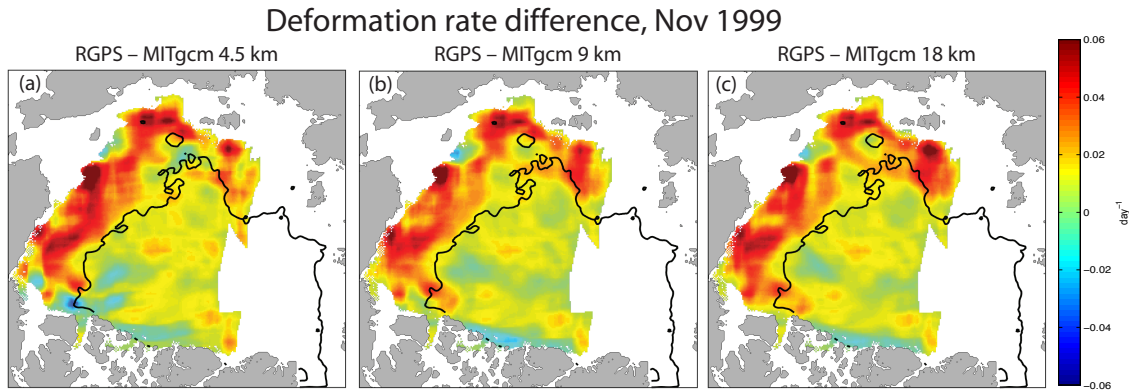

Figure 5. Smoothed (150 km) difference in deformation rate $\dot{D}$ between RGPS and model solutions with **(a)** 4.5, **(b)** 9, and **(c)** 18 km grid spacing. The largest differences occur in the seasonal ice zone outside the black contour.

and fracturing of the ice is very different from the perennial ice. These factors are not adequately included in the model.

In our model configuration, we use the typical ice pressure formulation P (or strength) of Hibler (1979):

$$P = P^* h\, e^{[C^*(1-C)]}. \tag{6}$$

The ice strength P depends linearly on the ice thickness h and exponentially on the ice concentration C. P^* and C^* are scaling constants for the ice strength parameterization. That P depends linearly on ice thickness h is a typical formulation for a VP or EVP sea-ice rheology with two ice classes and might not be the best representation of the P–h relationship. Models with more ice thickness classes often use a $P \propto h^{3/2}$ formulation (Rothrock, 1975; Lipscomb et al., 2007), which can be considered more realistic. As mentioned, there are, however, also other differences between the seasonal and perennial ice zone than the ice thickness. The proximity to open water in the MIZ, for example, will allow more cases of ice divergence at the ice margins than in the ice pack, which might be less well represented by the VP rheology. The examples for late winter in March and April 2000 in Sect. S2 show a reduced difference in divergence and shear for the seasonal ice zone. The ice has consolidated by then and the Arctic Basin is fully covered by sea ice, which reduces the mobility of the ice pack. In times of a changing Arctic environment, however, where seasonal sea ice is becoming the dominant ice type (Comiso, 2012), the problem of large discrepancies in simulated sea-ice deformation of the seasonal ice zone and MIZ will have an important impact.

3.1.2 Deformation rate time series

For this study RGPS observations from all 20 available periods of RGPS observations (i.e., 97 months, between November 1996 and May 2008) are used (Table 2). Figure 6a shows the period-averaged sea-ice deformation rate $\dot{D}$ and Fig. 6b the monthly mean seasonal cycle of $\dot{D}$. The months of September and October are not covered by RGPS data.

The time series of $\dot{D}$, $|\dot{\nabla}|$, $|\dot{\tau}|$, and $\dot{\zeta}$ behave very similarly. For simplicity we will therefore concentrate the discussion on the sea-ice deformation rate $\dot{D}$ (Fig. 6), but the statistics for all variables are presented in Table 3.

The RGPS deformation rate (black) is consistently higher than all of the 4.5 km (total mean +37 %), 9 km (+40 %), and 18 km (+44 %) simulations. The same is true for divergence, shear, and vorticity. The largest difference occurs for absolute divergence, which is 49–66 % lower than the RGPS data (Table 3). Overall, we conclude that the absolute amount of sea-ice deformation in our current sea-ice model setup is about 40 % too low in comparison to RGPS observations, and this underrepresentation of deformation is almost independent of model grid spacing during winter months. During summer months, however, the model performance differs depending on horizontal grid spacing, and the 4.5 km simulation shows the smallest difference to RGPS observations. This can be seen in the seasonal cycle in Fig. 6b, where during December to April the three model solutions are close to each other and agree within their standard deviation. Only during summer months (June–August), the 4.5 km solution shows a higher deformation rate than the 9 km solution, which again shows a higher deformation rate than the 18 km solution. The RGPS data show a clean, sinusoidal-like seasonal cycle with a clear minimum in March and maximum in August (likely the real maximum would occur during the unobserved month of September). For the 9 and 18 km model solutions the sinusoidal behavior of the seasonal cycle is less pronounced. They have a clear maximum during August but only a very weakly defined minimum in March. $\dot{D}$ is almost constant during January–May. The 4.5 km solution differs from this behavior and shows a clearer sinusoidal seasonal cycle than the other two model solutions with a defined minimum in February/March. That is, the 4.5 km solution again shows a better performance than the lower-resolution simulations.

The RGPS and all model deformation time series are highly correlated ($R^2 \approx 0.85$). The variability of the mod-
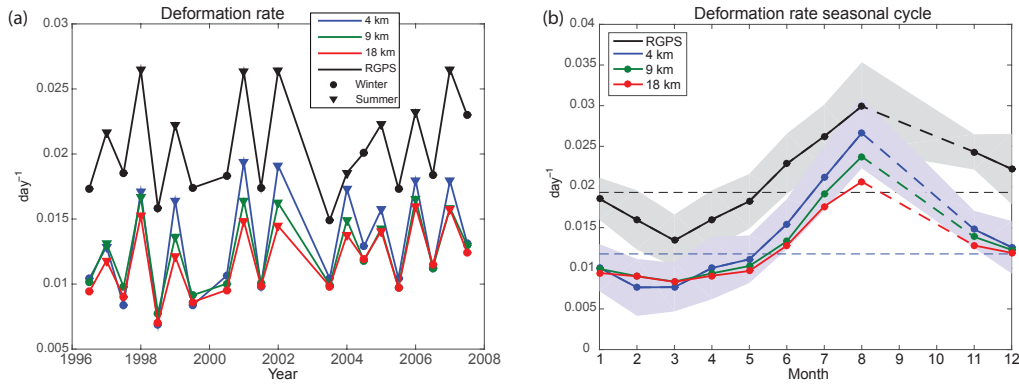
Figure 6. (a) Mean deformation rate $\dot{D}$ for all 20 RGPS periods and the corresponding modeled values. Circles mark winter periods and triangles summer periods; note that periods have different length (see Table 2). **(b)** Seasonal cycle of $\dot{D}$; shaded areas show standard deviations for RGPS and the 4.5 km solution (9 and 18 km solutions are similar); horizontal dashed lines show the mean calculated from the monthly time series; note that no data is available for September and October.

Table 3. Overview of some statistical parameters for the complete 97-month time series of RGPS and model sea-ice strain rate invariants. All units are $10^{-2}\,\mathrm{day}^{-1}$ if not otherwise indicated; $\pm$ values denote the standard deviation of the time series; "difference" is the difference between model and RGPS in %; and "correlation" is the correlation coefficient between the model and RGPS time series. The last rows summarize the power-law scaling exponents b for spatial scale and n for PDFs at 10 km scale (plus 95 % confidence bounds) discussed in Sect. 3.2 (no units, see also Eqs. 7 and 8).

| $\times 10^{-2}$		RGPS	4.5 km	9 km	18 km
Deformation rate $\dot{D}$	mean	1.9 ± 0.6	1.2 ± 0.6	1.1 ± 0.5	1.1 ± 0.4
	difference		-37%	-40%	-44%
	correlation		0.84	0.87	0.88
Absolute divergence $|\dot{\nabla}|$	mean	0.6 ± 0.3	0.3 ± 0.2	0.2 ± 0.1	0.2 ± 0.1
	difference		-49%	-63%	-66%
	correlation		0.79	0.83	0.84
Absolute vorticity $|\dot{\zeta}|$	mean	1.9 ± 0.5	1.2 ± 0.5	1.2 ± 0.4	1.2 ± 0.4
	difference		-33%	-34%	-37%
	correlation		0.75	0.78	0.79
Shear $\dot{\tau}$	mean	1.8 ± 0.5	1.1 ± 0.6	1.1 ± 0.5	1.0 ± 0.4
	difference		-35%	-37%	-41%
	correlation		0.84	0.87	0.87
Percentage Q of area containing highest 15 % of deformation rates	mean	$1.5\pm0.7\%$	$0.8\pm0.6\%$	$2.3\pm1.1\%$	$2.9\pm1.2\%$
	difference		-47%	49%	95%
	correlation		0.51	0.52	0.72
Spatial scaling exponent b for absolute divergence $|\dot{\nabla}|$	winter	-0.24 ± 0.03	-0.13 ± 0.03	-0.09 ± 0.03	-0.09 ± 0.04
	summer	-0.27 ± 0.01	-0.19 ± 0.03	-0.12 ± 0.03	-0.10 ± 0.03
Spatial scaling exponent b for shear $\dot{\tau}$	winter	-0.15 ± 0.04	-0.09 ± 0.04	-0.08 ± 0.04	-0.08 ± 0.05
	summer	-0.19 ± 0.05	-0.16 ± 0.05	-0.12 ± 0.05	-0.11 ± 0.06
Spatial scaling exponent b for deformation rate $\dot{D}$	winter	-0.16 ± 0.04	-0.10 ± 0.04	-0.08 ± 0.04	-0.08 ± 0.05
	summer	-0.19 ± 0.04	-0.16 ± 0.05	-0.12 ± 0.05	-0.11 ± 0.06
PDF scaling exponent n for absolute divergence $|\dot{\nabla}|$	winter	-3.26 ± 0.08	-2.12 ± 0.04	-2.9 ± 0.2	-3.3 ± 0.2
	summer	-2.4 ± 0.2	-2.5 ± 0.1	-2.6 ± 0.2	-2.9 ± 0.2
PDF scaling exponent n for shear $\dot{\tau}$	winter	-3.4 ± 0.1	-2.22 ± 0.04	-2.9 ± 0.1	-4.1 ± 0.2
	summer	-3.22 ± 0.07	-2.11 ± 0.08	-2.7 ± 0.1	-3.6 ± 0.2
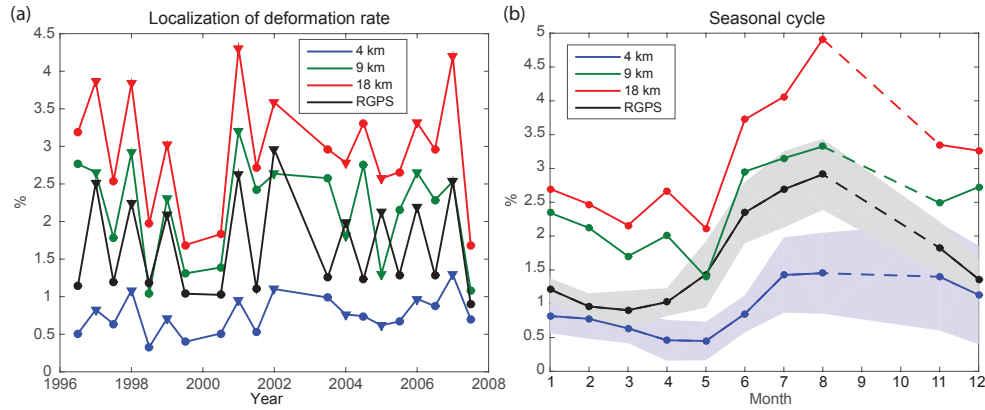
Figure 7. The percentage Q of area containing the highest 15 % of all sea-ice deformation rates shows the localization of deformation. **(a)** Time series showing the absolute percentage Q for RGPS data (black) and model solutions with 4.5 (blue), 9 (green), and 18 km (red) grid spacing for all 20 RGPS periods. Circles mark winter periods and triangles summer periods; note that periods have different lengths (see Table 2). **(b)** Seasonal cycle of Q; shaded areas show standard deviations for RGPS and the 4.5 km solution (9 and 18 km solutions are similar); note that no data is available for September and October.

eled deformation rate is slightly smaller but comparable to the observed RGPS variability. The standard deviation σ of the monthly $\dot{D}$ time series (not shown) is with $\sigma = 0.6 \times 10^{-2}$ day^{-1} comparable to the standard deviations of the 18, 9, and 4.5 km solutions ($\sigma = 0.4$ to 0.6×10^{-2} day^{-1}, see Table 3). Again the 4.5 km solution shows the highest variability and performs best.

3.1.3 Localization of deformation

As seen in Sect. 3.1.2, the absolute magnitude of sea-ice deformation in the model is much too low. Nevertheless, in Sect. 3.1.1 it was shown that the modeled sea-ice deformation distribution gets more similar to the observed one if the model grid spacing is decreased. In particular, more and better-confined LKFs appear for smaller grid spacing (e.g., Fig. 4). To show this change in the sea-ice deformation distribution more quantitatively, we now look at the "localization" of the deformation rate (Marsan et al., 2004). Following Stern and Lindsay (2009) we calculate the area fraction Q, which contains the highest 15 % of all sea-ice deformation rates. Q is calculated as

$$\dot{D}_1 \geq \dot{D}_2 \ldots \dot{D}_{n-1} \geq \dot{D}_n,$$

$$\sum_{i=1}^{p} \dot{D}_i = 0.15 \sum_{i=1}^{n} \dot{D}_i,$$

$$Q = \sum_{i=1}^{p} A_i \bigg/ \sum_{i=1}^{n} A_i,$$

where $\dot{D}_i$ are the individual Lagrangian deformation rate observations sorted by their magnitude, starting with the highest. A_i are the accordant triangle areas. The number of observations n is identical for all model simulations and the RGPS

data. This measure is independent of the absolute amount of deformation rate.

The smaller the percentage Q gets, the more localized the deformation is distributed. If the deformation rates were evenly distributed, the highest 15 % would also occupy 15 % of the area. We will see that Q is indeed much smaller than that. Figure 7a shows the time series of Q for all 20 RGPS periods for the three model solutions and the RGPS data and Fig. 7b the seasonal cycle of Q (also see Table 3 for statistics).

Sea-ice deformation in both the RGPS observations and all three model solutions is very localized. The highest 15 % of all deformation rates Q is only occupying between 0.8 and 2.9 % of the total area for all models and data. Q decreases with decreasing model grid spacing. There is a big difference in Q for the 4.5 km simulation ($\overline{Q} = 0.8$ %) compared to Q of the 9 and 18 km simulations ($\overline{Q} = 2.3$ % and $\overline{Q} = 2.9$ %, respectively). The mean $\overline{Q} = 0.8$ % of the 4.5 km simulation is even significantly lower (-47 %) than the localization $\overline{Q} = 1.5$ % of the RGPS observations. This shows that the sea-ice deformation distribution got considerably more confined for the 4.5 km simulation compared to the other two lower-resolution simulations, which are 49 and 95 % higher than the RGPS data, respectively. This can also be seen in the examples of Figs. 2–4, which show a strong increase in the number of LKFs when the grid spacing is reduced from 18 and 9 to 4.5 km. The strain rate distributions for the 18 and 9 km simulations are much more similar. This increase in LKFs is confirmed here by the very strong localization Q for the 4.5 km solution. It is not clear why the change in Q is so big for the 4.5 km solution compared to the other two solutions. Despite the big difference in the mean deformation rate compared to the RGPS data, the 4.5 km simulation is able to reproduce the fraction of the total area, in which

the strong sea-ice deformation events are concentrated very well. The events are even too confined compared to RGPS. Additionally, the seasonal cycle of Q in Fig. 7b is similar for the 4.5 km solutions compared to RGPS observations. The increase in Q in summer, however, comes later and stays at lower values for the 4.5 km solution. The seasonal cycle for the 18 and 9 km simulation is also similar to RGPS in terms of timing but the magnitude is a bit enhanced. The standard deviations of Q for the monthly time series are similar for RGPS and the 4.5 km simulation (0.7 and 0.6 %, respectively). For the 18 and 9 km model solutions, however, the standard deviations are about double that (1.1 and 1.2 %, respectively). Especially the 18 km model simulation shows much higher Q values during summer, which hints towards a degraded performance during summer.

In summary, sea-ice deformation in the model solution with the finest grid spacing of 4.5 km is most confined and localized, as had already been seen in the examples of Sect. 3.1.1 and the Supplement). One has to keep in mind, however, that the absolute model deformation rate is about 40 % lower than that of the observations. From the three model solutions, the 4.5 km simulation can be considered most consistent with the RGPS observations.

3.2 Power-law scaling of deformation rates

Sea-ice strain rates do not scale linearly in space and time. Instead, the scaling follows a power law. Some details about the nature of this scaling dependence are given in, for example, Weiss (2003, 2013). In Sects. 3.2.1 and 3.2.2 we will compare the power-law scaling of the model solutions with the RGPS data based on length scale and their respective probability density functions (PDFs). There is some discussion in current literature on how well the VP ice rheology is able to reproduce this power-law scaling (e.g., Girard et al., 2009). In Sect. 3.2.3 we use the power-laws scaling dependence to compare the sea-ice deformation rate for three model solutions with different grid spacing.

3.2.1 Dependence on length scale

The magnitude of sea-ice strain rates and their invariants depends on the spatial scale over which they are determined. In this section we use the absolute divergence $|\dot{\nabla}|$ and shear rate $\dot{\tau}$ as examples, but similar relationships exist for the deformation rate $\dot{D}$ and vorticity $\dot{\zeta}$. For absolute divergence $|\dot{\nabla}|$ and length scale L over which $|\dot{\nabla}|$ is determined, this power-law scaling can be expressed as

$$|\dot{\nabla}| \approx dL^b. \tag{7}$$

For $\dot{\tau}$ the equation is equivalent. b is the scaling exponent and d a constant of proportionality, which can be interpreted as mean deformation rate at a given base scale. We use the consistent Lagrangian strain rate dataset described in Sects. 2.3 and 2.4 to compare RGPS observations with model solu-

tions. Following the procedure described in Stern and Lindsay (2009), strain rates at different spatial scales are calculated. The seven nominal length scales $L^* = 10$, 20, 50, 100, 200, 500, and 1000 km are used. The initial length scale of the RGPS data is 10 km, and therefore this is the smallest scale that can be obtained. We obtain those strain rates as follows:

- All Lagrangian cells within a 5-day window are aggregated on a regular grid with grid cell size L^*. All Lagrangian cells whose center coordinate fall within a grid cell form the aggregate for that cell.

- A filter is applied: the time interval Δt of the individual Lagrangian cells must be between 2 and 5 days and their individual area between 25 and 100 km^2. The total area of the remaining aggregated cells must be greater than $0.75 L^{*2}$.

- For each aggregate, mean strain rates ($\partial u/\partial x$, $\partial u/\partial y$, etc. – see Eq. 1) are computed from the individual strain rates in the aggregate by using the cell areas as weight. The deformation invariants ($\dot{\nabla}$, $\dot{\tau}$) for the aggregates are then computed with those mean strain rates.

- The actual length scale L for each aggregate is determined by the square root of all cell areas.

Figure 8 shows the absolute divergence $|\dot{\nabla}|$ and shear rate $\dot{\tau}$ versus the length scale L for RGPS observations and the three model solutions with 4.5, 9, and 18 km grid spacing on a log–log scale. The dataset was split in the winter and summer RGPS periods (Table 2). The averages of $|\dot{\nabla}|$ and $\dot{\tau}$ for the seven nominal scales 10, 20, 50, 100, 200, 500, and 1000 km are marked by symbols.

The RGPS observations and all three model solutions follow a power-law scaling, both during winter and during summer. Figure 8 shows least square fits for the seven mean values between 10 and 1000 km as dashed lines. While both the observations and model solutions follow a power law, the inclinations of the fit, i.e., the scaling exponent b in Eq. (7) is steeper for RGPS than for the model solutions. All b values (and uncertainty estimates) are summarized in Table 3, including values for deformation rate $\dot{D}$.

For absolute divergence $|\dot{\nabla}|$ the exponent b for RGPS is -0.24 ± 0.03 during winter and -0.27 ± 0.01 during summer. The magnitude of b for the model solutions is lower. The b values of the 4.5 km solution are -0.13 ± 0.03 for winter and -0.19 ± 0.03 for summer, which is closest to the RGPS data. The 9 and 18 km solutions show similar b values that differ strongly from the RGPS ones (-0.09 during winter and -0.12 to -0.10 during summer).

For shear $\dot{\tau}$ the situation is similar. During winter the RGPS b value is -0.15 ± 0.04, and during summer $b = -0.19 \pm 0.05$. The b value magnitude for the model solutions is again smaller. During winter all model solutions have similar b exponents (-0.09 ± 0.04 for the 4.5 and
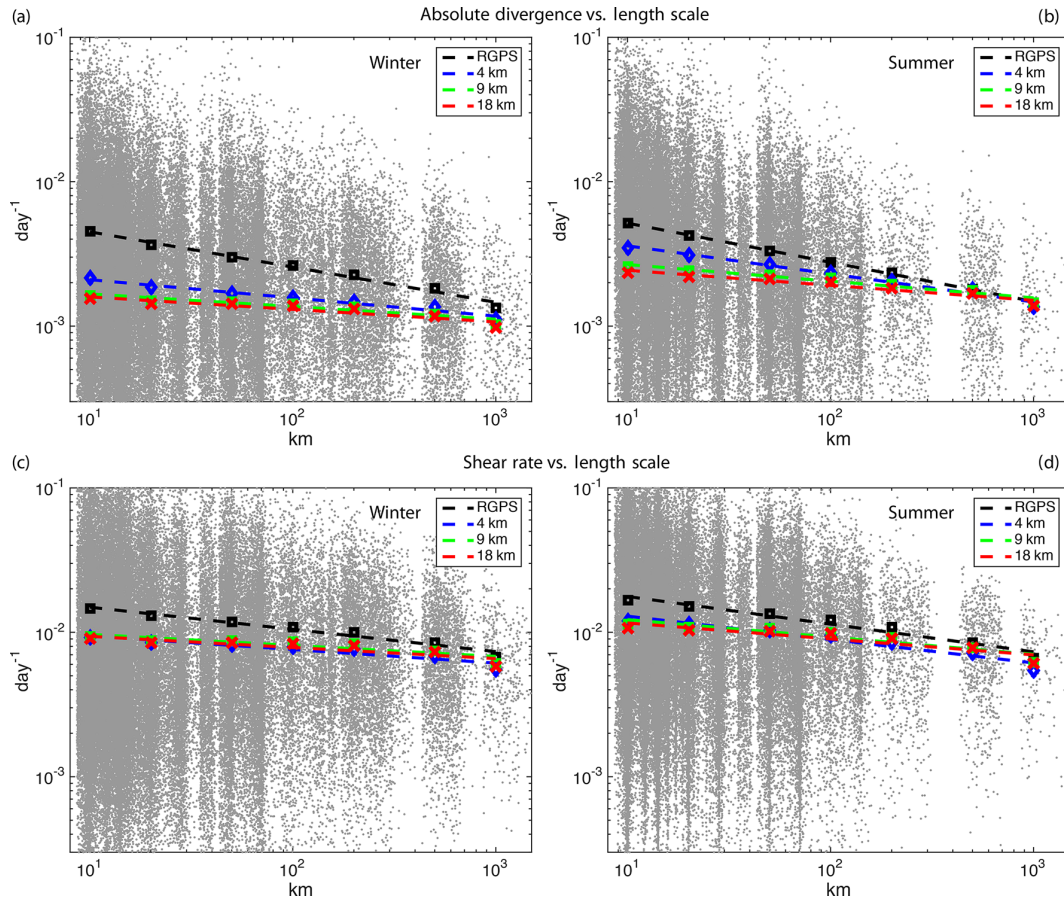
Figure 8. Scaling properties of absolute sea-ice divergence $|\dot{\nabla}|$ **(a, b)** and shear rate $\dot{\tau}$ **(c, d)** for RGPS and model solutions for all winter (November–May; **a, c**) and summer (May–August; **b, d**) periods. For length scales of 10, 20, 50, 100, 200, 500, and 1000 km, the ice divergence and shear from the Lagrangian cells were aggregated over 5-day periods. Individual data points for the RGPS dataset are shown in gray. Mean values for the seven different length scales are marked with symbols. Dashed lines are least square fits to the seven mean values from 10 to 1000 km. Note the logarithmic axes scaling.

-0.08 ± 0.05 for the 9 and 18 km solutions). During summer the 4.5 km solution again comes closest to RGPS with $b = -0.16 \pm 0.05$, while the 9 and 18 km solutions have b exponents of -0.12 ± 0.05 and -0.11 ± 0.06, respectively.

Our estimates of b for RGPS agree well with previous estimates from, for example, Marsan et al. (2004) and Stern and Lindsay (2009), who report for the deformation rate $\dot{D}$ a b value of ≈ -0.2 during winter and ≈ -0.3 during summer in the Arctic. We obtain b values of somewhat lower magnitude (-0.16 for winter and -0.19 for summer; see Table 3). In contrast to these studies we, however, use an anisotropic spatial filter to reduce sampling noise (Sect. 2.4). Our b values for the unfiltered RGPS data of $b = -0.22$ and -0.25 for summer and winter, respectively, agree very well with previous studies (see Sect. 3.3 and the Supplement). A similar change of b for filtered vs. unfiltered RGPS data was reported by Bouillon and Rampal (2015a).

More importantly, for the model solutions our results do not agree with previous studies. Our model solutions repro-

duce the power-law scaling properties very well. While the b values are different, the quality of the fit for the model solutions and RGPS data are very similar and very good for both (see Fig. 8). We do not observe the strong divergence from power-law scaling for models with VP ice rheology reported by Girard et al. (2009).

3.2.2 Probability density function

Another way to look at the power-law scaling behavior of sea-ice deformation rates is by comparing probability density functions (PDFs) obtained from model solutions and RGPS data. The PDFs for observed sea-ice strain rates follow a power law. For example, Girard et al. (2009) report that the PDF of RGPS strain rates during January to March 1997 follows a linear relation in log–log space:

$$p(|\dot{\nabla}|) \propto |\dot{\nabla}|^n. \tag{8}$$

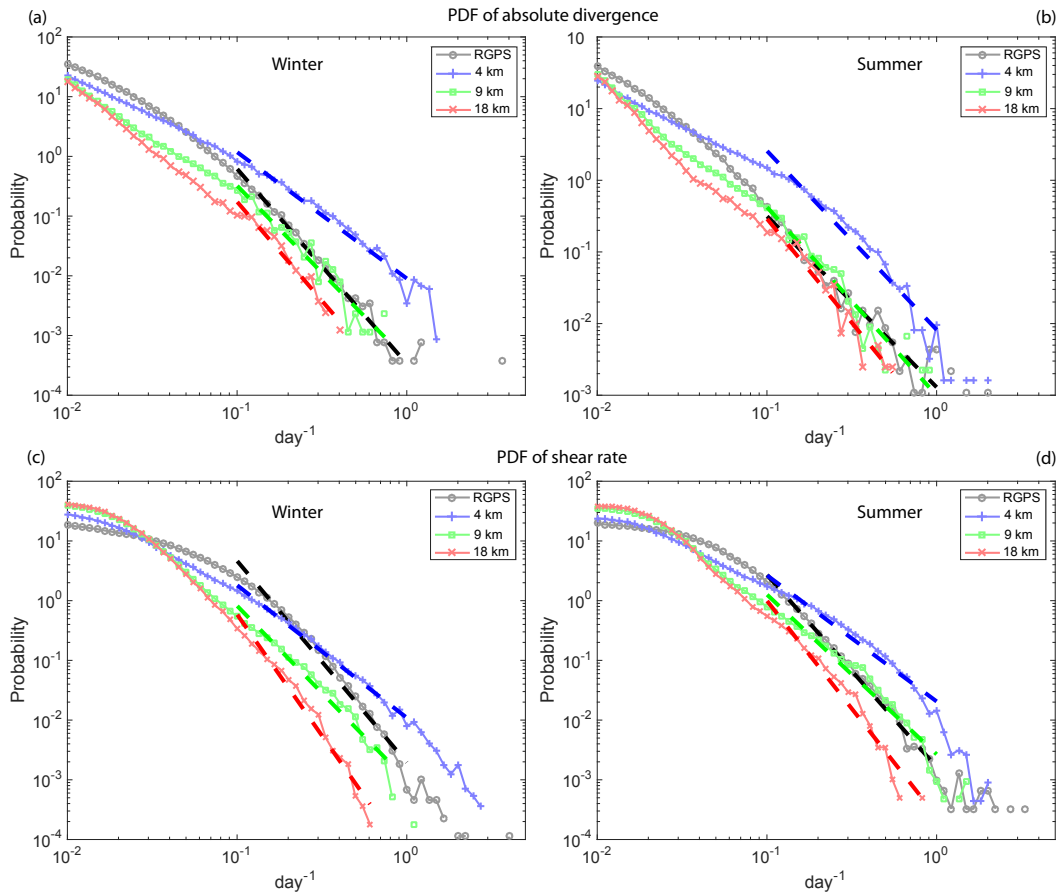For the comparisons, the same 5-day aggregated RGPS and model datasets described in the previous Sect. 3.2.1 were

Figure 9. Probability density function of absolute sea-ice divergence $|\dot{\nabla}|$ **(a, b)** and shear rate $\dot{\tau}$ **(c, d)** for a length scale of 10 km based on 5-daily aggregated Lagrangian cells for all winter (November–May) and summer (May–August) periods for RGPS and model solutions. Dashed lines are least square fits to the approximately linear part of the PDFs between 0.05 and 1.0 day^{-1}. Note the logarithmic axes scaling.

used. We show results obtained for the nominal length scale $L^* = 10$ km. Results for the other length scales are similar. PDFs at lower resolutions are even a bit smoother, but qualitatively the conclusions are the same. PDFs p for absolute divergence $|\dot{\nabla}|$ and shear rate $\dot{\tau}$ are then calculated for all winter (11 years) and summer (9 years) RGPS periods (see Table 2). Figure 9 shows the PDFs for the three model solutions with 4.5 (blue), 9 (green), and 18 km (red) grid spacing and the RGPS data (black) on a log–log scale. Table 3 summarizes the obtained n exponents including uncertainty estimates.

A linear least squares regression was applied to the PDFs in log–log space for the range 0.1–1.0 day^{-1}, shown as dashed lines in Fig. 9. The same range was used for all four plots. For very small and large deformation rates outside that range, the RGPS PDFs diverge from the power-law relationship. The accuracy of the RGPS observations is about 100 m and noisy at that scale. Low deformation rates therefore could be underrepresented in the RGPS PDF, which potentially could explain the deviation from a straight line for low deformation rates in Fig. 9. For very high deformation

rates the low number of data points causes artificial variability in the PDFs.

The slope of $|\dot{\nabla}|$ and $\dot{\tau}$ for both the winter and summer RGPS PDF is $n \approx -3.3$, and only the summer slope of $|\dot{\nabla}|$ diverges with $n = -2.4$ (more values in Table 3). This is consistent with, but more negative than, what is found in Marsan et al. (2004) and Girard et al. (2009), who report winter RGPS PDF slopes of about -2.5 for strain rates at the ≈ 10 km scale. Again one needs to consider that our datasets are spatially filtered (Sect. 2.4), which will impact the statistical values but not the overall behavior. All model solutions show a power-law scaling of the PDFs similar to the RGPS data for both $|\dot{\nabla}|$ and $\dot{\tau}$. The magnitude of n for the model solutions always follows the same pattern: it is lowest for the 4.5 km solutions, followed by the 9 km one, and highest for the 18 km simulation. The scaling exponents of the 9 km solution agree best with RGPS ones and often overlap within the uncertainty estimates (Table 3). The 4.5 km solution always has a shallower and the 18 km one a steeper slope than the RGPS data for both $|\dot{\nabla}|$ and $\dot{\tau}$.

In most cases the three model solutions show a power-law scaling behavior over an even larger absolute range than the RGPS data (approximately 10^{-2} to $1\,\text{day}^{-1}$ for divergence). During summer, the model solutions PDFs are more variable and the 4.5 km solutions especially diverge from the power-law relationship for both $|\dot{\nabla}|$ and $\dot{\tau}$. The model solutions show a higher probability for small shear rates $\dot{\tau}$ than the RGPS data as can be expected since the deformation rates are about 50 % lower as discussed in Sect. 3.1.2.

Overall the slopes of the PDF tails for simulated and observed RGPS absolute divergence and shear rates show good agreement. The observed and simulated power-law exponents n are of the same order during both winter and summer months (RGPS: $n \approx -3.1$; model solutions: $n = -2.2$ to -3.5). During winter and summer the PDFs of the 9 km solution agree best with the RGPS data, but all model solutions show good agreement. Again, we do not observe the strong deviation from power-law scaling reported by Girard et al. (2009) for model simulations using the VP and EVP sea-ice rheology. In our model setup the used VP rheology seems to be able to reproduce a realistic distribution of deformation rates, which follow a power-law relationship.

3.2.3 Comparing models with different grid size

In this section, we examine whether sea-ice deformation rates in the three model simulation with different horizontal grid spacing follow a similar power-law scaling as found in observations and as discussed in Sect. 3.2.1. The motivation is to make the deformation rates of the three model solutions directly comparable to each other. We will show that this is not possible generally speaking.

It is a common problem when one wants to compare sea-ice deformation rates from different model simulations. These model simulations then, in general, have a different grid resolution, and a direct comparison is not possible due to the different length scales involved. We will explore if the power law in Eq. (7) with a constant exponent b can be used to compare mean absolute deformation rates of model solutions with different grid spacing as it was suggested by, for example, Stern and Lindsay (2009). We use the deformation rate $\dot{D}$ here again to not discuss the three different strain rate invariants separately, which give similar results.

Due to the different averaging length scale L, one would not expect $\dot{D}$ to be the same for model solutions with different grid spacing. In Sect. 3.1 we avoided this problem by interpolating the model solutions to the RGPS Lagrangian locations. Here we keep the spatial resolution of the three model simulation and calculate all strain rates on the three original model grids with 4.5, 9, and 18 km resolution, respectively. At least for the model solutions with higher or similar spatial scale as the RGPS data, i.e., the 4.5 and 9 km solutions, this will create comparable datasets. Due to its lower spatial scale, the 18 km solution cannot, in theory, fully

recreate the RGPS data, regardless of the sea-ice rheology formulation.

Figure 10a shows the 1992–2008 time series of the mean sea-ice deformation rate $\dot{D}$ in the complete model domain shown in the Fig. 1a inset. Different from the previous sections and, for example, Fig. 6, the complete model domain is now considered, and not only the areas covered by RGPS data. As expected the deformation rate for the 4.5 km model solution (blue, mean $\dot{D}_{4.5\,\text{km}} = 0.123\,\text{day}^{-1}$) is consistently higher than that of the 9 km solution (green, mean $\dot{D}_{9\,\text{km}} = 0.085\,\text{day}^{-1}$, -31 % compared to $\dot{D}_{4.5\,\text{km}}$), which itself is higher than that of the 18 km solution (red, mean $\dot{D}_{18\,\text{km}} = 0.054\,\text{day}^{-1}$, -36 % compared to $\dot{D}_{9\,\text{km}}$). The variability from year to year of the mean deformation rate is large, especially during summer. Some years, e.g., 1997–1999, have clearly reduced summer deformation rates in comparison to, for example, the beginning of the 1990s or 2007 and 2008. The deformation rate during 2008, both during summer and winter, is the highest of the complete time series (Fig. 10a).

We assume that the model deformation rate $\dot{D}$ follows the same power law as given in Eq. (7) and apply a least squares fit in log space to Eq. (7):

$$\log(\dot{D}_i) = \log(d) + b\log(L_i)\ (i = 4.5, 9, 18\,\text{km}),$$

with daily mean deformation rates $\dot{D}_i$ from model solutions with grid spacing $L_i = 4.5$, 9, and 18 km. The deformation rates for all sea-ice-covered grid cells ($C > 0$) is averaged and b calculated on a daily basis. For all sea-ice-covered areas in the model domain and for the complete time series, the power-law scaling exponent b is estimated to be -0.54. The exponent is different from the ones found in Sect. 3.2.1. First, a different method is used here, but more importantly a different regional domain is covered. The model domain used here contains the complete MIZ and low ice concentrations, which allow more free-drift cases that result in a more negative b exponent.

Figure 10b shows the deformation rate time series for the three model solutions normalized to a length scale of $L = 10\,\text{km}$, using the estimated scaling exponent $b = -0.54$ and Eq. (7). The length scale of 10 km was chosen to be comparable to the RGPS data. Using this scaling, the three time series become much more similar than the original ones in Fig. 10a. If shown in detail, however, some quite large differences remain. For example, the mean $\dot{D}$ of the 9 km simulation is now higher than that of the other two simulations; and the standard deviations of all three simulation are still different (not shown: the standard deviation of the 18 km simulation is more than $0.05\,\text{day}^{-1}$ smaller than that of the 9 and 4.5 km simulations).

These differences imply that a single, constant scaling exponent b is not sufficient to make the strain rates of the three model solutions comparable. b varies seasonally and regionally. Figure 10c and d show, respectively, the dependence of sea-ice deformation rate $\dot{D}$ on sea-ice concentration C
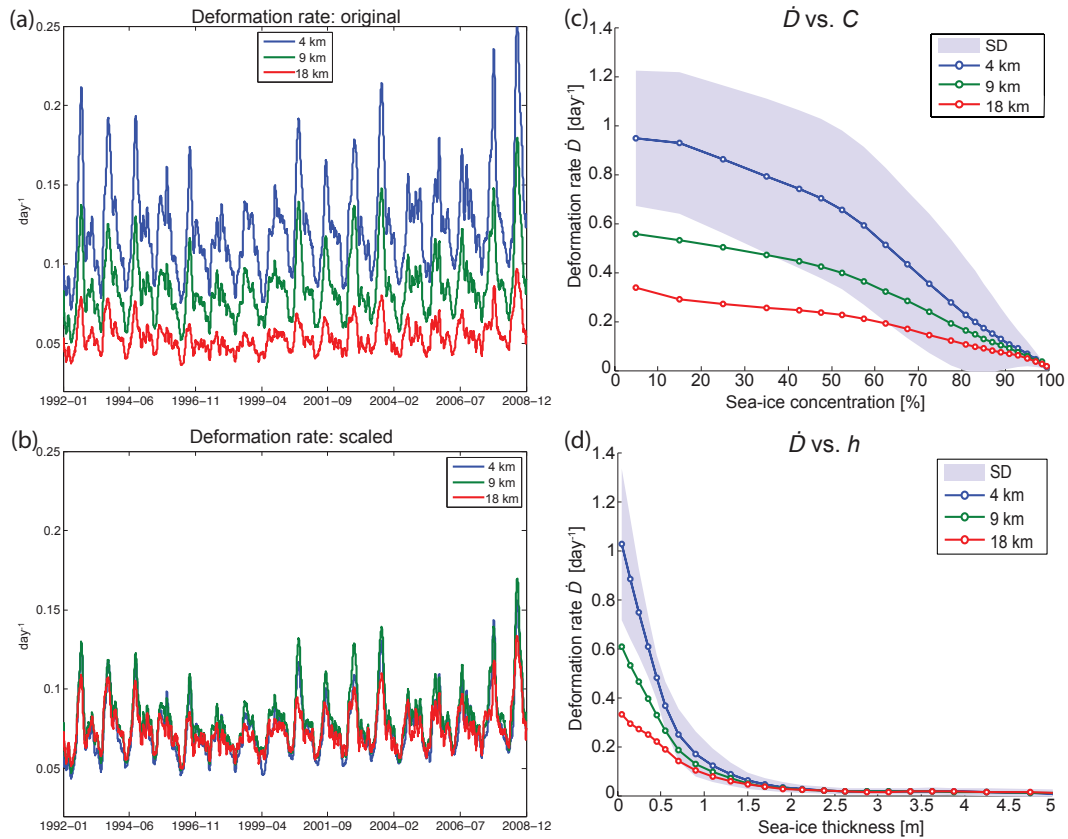
Figure 10. (a) Time series 1992–2008 of mean deformation rate $\dot{D}$ in the complete model domain (see Fig. 1) for model runs with 4.5 (blue), 9 (green), and 18 km (red) grid spacing. **(b)** as **(a)** but for deformations normalized to a 10 km scale using Eq. (7) with $b = -0.54$. All curves are 1-month running means. **(c)** and **(d)** show, respectively, the dependence of sea-ice deformation rate $\dot{D}$ on sea-ice concentration C and sea-ice thickness h for the three model integrations. Blue shaded color areas mark ± 1 standard deviation for the 4.5 km solution.

and sea-ice thickness h for the three model solutions during the complete 1992–2008 time series. In Fig. 10c, the deformation rate decreases with increasing sea-ice concentration for all three model runs and $\dot{D}$ approaches zero linearly for 100 % ice-covered grid cells. Additionally, for increasing ice thickness in Fig. 10d, the deformation rate decreases, but here the deformation rate decreases exponentially. For sea-ice thickness above 2 m, $\dot{D}$ is near zero. It has to be noted that the ice thicknesses h are the effective ice thicknesses of a complete grid cell, which also can contain open water ($C < 100\%$).

From Fig. 10c and d, it becomes clear that the scale dependence is much stronger for small ice concentrations and thicknesses than for large ones. The scaling exponent b gets more negative for weaker sea ice and approaches zero for very strong sea ice, i.e., thick ice and 100 % ice concentration (see Eq. 6 for how the ice strength dependencies are incorporated in the model).

There are additional external factors that influence b. For free-drift ice, b gets more negative as can be seen by the strong dependence on C. Therefore, the surrounding geography, i.e., landmasses, influence the scaling exponent with

b values closer to zero in channels and near the coast, where the ice cannot drift freely. The estimated power-law scaling factor b represents the balance between all these factors. That is, sea-ice concentration, thickness, and geographic location are important contributors to the estimated scaling exponent.

The factors mentioned in the last paragraph also explain why the scaling exponent $b = -0.54$ found here for the three simulations is significantly lower than the values of b of about -0.2 found for RGPS data in Sect. 3.2.1 or by Stern and Lindsay (2009). There are other factors influencing the deformation rate for the different model solutions compared to the averaging of different scales in Sect. 3.2.1, but the different regions covered will have the dominating influence. In the model, the values of b between -0.3 and -0.2 are typical for ice concentrations $\geq 80\%$. These are typical ice concentrations for the RGPS region, which rarely extends to the marginal ice zones with low ice concentrations. If the calculation of the scaling exponent b in the model is restricted to the region covered by RGPS data, a mean b value of ≈ -0.2 is found, which is comparable to the b values found for RGPS data. This scaling exponent, however, is not applicable to the complete Arctic. For this reason, it is difficult to compare
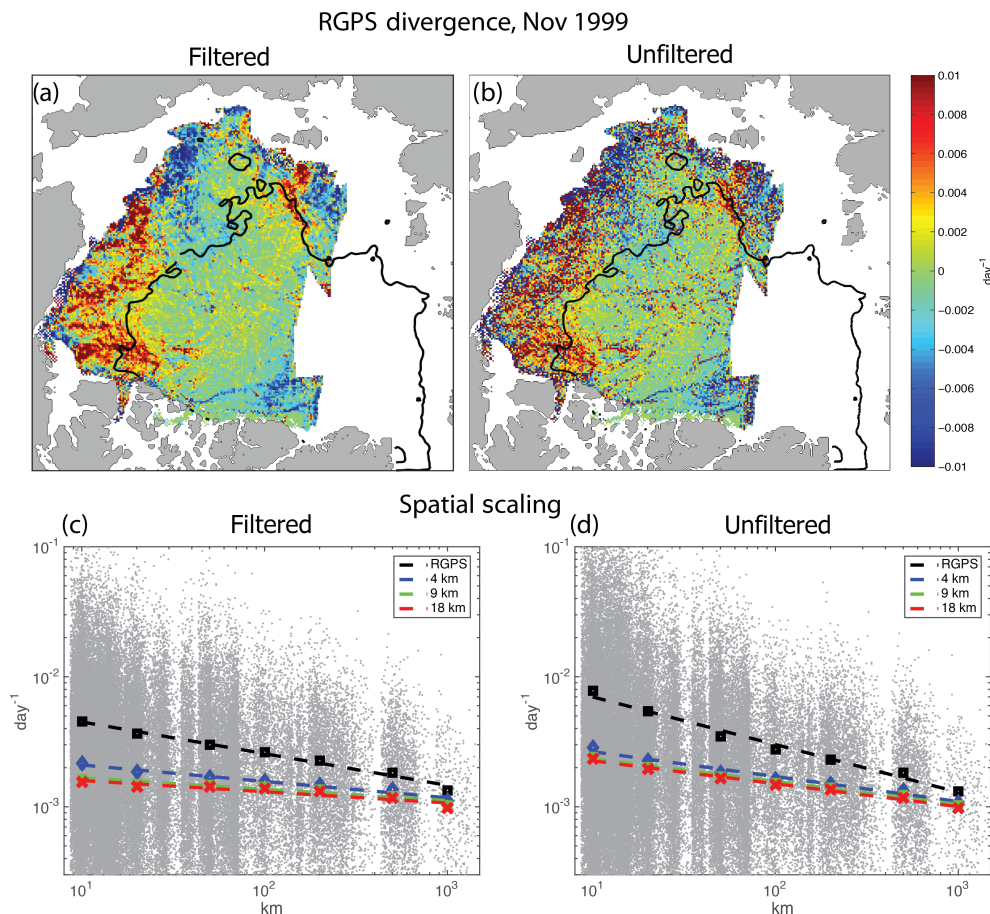
Figure 11. Comparison of filtered and unfiltered datasets using the anisotropic smoother described in Sect. 2.4. **(a)** RGPS divergence for November 1999. This is the same sub-figure as in Fig. 2a. **(b)** as **(a)** but using the unfiltered RGPS data. The divergence field appears more noisy. **(c)** The spatial scaling of absolute divergence for the RGPS data and model solutions based on the filtered datasets for all winter periods. This is the same sub-figure as in Fig. 8a. **(d)** as **(c)** but for the unfiltered datasets. The slopes are shallower for the filtered datasets, and the quality of the fit improves.

sea-ice deformation rates obtained at different spatial scales. For direct comparison, strain rates need to be calculated for identical areas, as was done in Sect. 2.3. At the very least, for meaningful statistical comparisons, the different scaling behavior for different ice concentrations needs to be considered.

In summary, the three simulations with different horizontal grid spacing, i.e., different resolved spatial scales, follow a similar power-law scaling as that estimated using RGPS and buoy observations. We attribute most of the differences between simulated and observed scaling factor b to the different sea-ice concentration and thickness ranges of each dataset. The simulated power-law scaling strongly depends on ice strength, which itself depends on ice concentration and thickness. For strong sea ice, all model solutions converge to comparably small deformation rates. In reality, i.e., for the observations, ice strength depends on many more factors, e.g., floe size and level of fragmentation and fracturing. The power-law scaling exponent b therefore varies in space

and time. Due to all these factors, in most cases it will not be possible to directly compare the deformation rates of model solutions with different grid spacing based on the power-law relationship.

3.3 Comparison filtered vs. unfiltered datasets

The anisotropic smoothing filter described in Sect. 2.4 will change the statistical properties of both the RGPS dataset and model solutions. Figure 11 shows, for example, how the filter changes the sea-ice divergence fields and spatial scaling properties. More examples are given in the Supplement, where all figures from the main text are reproduced based on the unfiltered datasets. For the comparison we obtain similar results as described in Bouillon and Rampal (2015a).

The goal of the anisotropic filtering is to keep the shape of the LKFs but reduce the noise introduced by the sampling of the Lagrangian cells (see Sect. 2.4). Figure 11a and b clearly demonstrate that the divergence fields are significantly im-

proved by applying the filter. One would expect that a particular LKF is either divergent or convergent, i.e., either a lead is opening or closing. The unfiltered divergence field in Fig. 11b shows many LKFs with divergent and convergent grid cells next to each other. For the filtered divergence field in Fig. 11a, LKFs are mainly either divergent or convergent, which is a much more physical result. The large-scale divergence pattern, however, stay the same for the filtered and unfiltered divergence fields and all other strain rates.

As a result of the smoothing, the absolute divergence (and also the magnitude of all other strain rates) gets significantly reduced. This reduction is 50 % higher for RGPS divergence, but the shear, vorticity, and deformation rate also decreases by about 30 % (compare Table 3 with Table S1 in the Supplement). For the model solutions the decrease is 47 and 15 %, respectively, smaller.

This reduction in divergence magnitude can be seen in Fig. 11c and d, where the absolute divergence is much lower for the filtered RGPS data and model solutions than for the unfiltered ones (mind the logarithmic scale). This reduction, however, is not uniform at all spatial scales because the anisotropic filter smooths only regionally within a given kernel size (see Sect. 2.4). For large spatial scales the filtered and unfiltered results therefore converge to each other, and at the 1000 km scale the mean divergence is almost the same (see Fig. 11c and d). As a result the gradient of the log–log fit, i.e., the scaling exponent b, is much shallower for the filtered datasets. The quality of the fit, however, gets better for the filtered datasets: the averages for the seven investigated spatial scales between 10 and 1000 km lay almost perfectly on the fit line for both RGPS data and model solutions in case of the filtered datasets. For the unfiltered datasets the fit is still very good, but some deviations can be observed for the RGPS observations.

The anisotropic filter described in Bouillon and Rampal (2015a) improves the representation of the deformation fields for both RGPS data and model solutions. The absolute numbers and statistics obtained from the filtered deformation fields should be more realistic and physical than the unfiltered ones. One will obtain quite different numbers for the means and scaling exponents for the filtered datasets as was, for example, demonstrated here. The general behavior of the deformation field and their statistical properties, as for example the power-law scaling, does not qualitatively change for the filtered data. The conclusions drawn from a comparison between different datasets, like in our example between the RGPS observations and model simulations, would be very similar for the filtered and unfiltered datasets (compare the results here and in the Supplement). In most cases the filter will affect different datasets in a similar way, and for comparative studies the results, qualitatively, should stay similar. Moreover, the filtered datasets will provide more consistent and physically more plausible results for all sea-ice deformation fields.

4   Summary and concluding remarks

Sea-ice deformations from coupled Arctic Ocean and sea-ice simulations with horizontal grid spacing of 18, 9, and 4.5 km were compared to RGPS satellite observations during the 1992–2008 period (Sect. 3). Lagrangian sea-ice drift was reconstructed from the three model solutions for a direct comparison with the RGPS data (Sect. 2.3), and noise related to the sampling of the Lagrangian data points was removed by an anisotropic filter (Sect. 2.4). Sea-ice strain rate invariants divergence and shear as well as vorticity and deformation rate were calculated in the same way for the three simulations and for satellite observations from the Lagrangian ice drift datasets. Even though the viscous–plastic dynamic sea-ice model with elliptical yield curve is able to produce what appears to be linear kinematic features, the orientation and spatial density of these LKFs are very different from what is observed in the RGPS data. For the 4.5 km simulation, however, many more and more confined LKFs are visible compared to the two lower-resolution simulations. A small model grid spacing seems to be essential to represent LKFs using VP sea-ice rheology. The mean sea-ice deformation rate, however, is between 37 and 44 % lower in all simulations than in the RGPS data. The largest difference occurs for the magnitude of divergence, which is 49–66 % too low (Table 3). Additionally, the large-scale shear pattern is not well reproduced in the model solutions (Fig. 4). In addition the LKFs occur less frequently in the simulations. Of the three model solutions, the one with the smallest grid spacing of 4.5 km has characteristics closest to RGPS observations.

While RGPS sea-ice deformation data show a clear discrimination between the thinner seasonal sea ice with more deformation and the thicker perennial sea ice, the model deformation zones are mainly confined to a few LKFs at the ice margins. Differences are largest for seasonal sea ice, where the model strongly underestimates sea-ice deformation. This suggests a shortcoming of the ice rheology, e.g., the linear dependence between ice strength and ice thickness. Model solutions with smaller grid spacing, however, result in more small-scale deformation features. In particular, the 4.5 km simulation has more LKF-like features in the Central Arctic than the coarser-resolution simulations, and, visually, the spatial distribution of these LKF-like features agrees better with RGPS observations. This improved realism is evaluated by computing the percentage Q of sea-ice area containing the highest 15 % of sea-ice deformation rates, which is a measure of how confined the deformation processes are. For this metric, the 4.5 km model solution shows the most confined deformation features with a Q value of 0.8 %, which is even lower than the RGPS data with $Q = 1.5$ %. The 9 and 18 km simulations have much higher Q values of 2.3 and 2.9 %, receptively – i.e., the deformation features are much less confined. These differences in small-scale deformation features can be important because ocean-to-atmosphere heat transfer tends to occurs on small scales. For example, the heat

flux from narrow leads can be twice as high as that from larger leads (Marcq and Weiss, 2012), and ocean upwelling events caused by sea-ice shear motion happen on small scales (McPhee et al., 2005).

In Sect. 3.2 we compare the power-law scaling behavior of the three model solutions with the RGPS observations. Both the RGPS data and all model solutions show a clear power-law dependence of the absolute divergence $|\dot{\nabla}|$ and shear rate $\dot{\tau}$ to the length scale L. The scaling exponent b for the RGPS data, however, is about twice as negative as for the 9 and 18 km model solutions (e.g., for $|\dot{\nabla}|$: $b \approx -0.25$ for RGPS and $b \approx -0.1$ for the 9 and 18 km model solutions). The b value of the 4.5 km simulation comes closest to the RGPS value (e.g., for $|\dot{\nabla}|$: $b \approx -0.16$). The power-law scaling for the tail of the probability density functions of absolute divergence and shear for the three model solutions is similar to the RGPS data. During both summer and winter, the power-law scaling exponent n for the models ($n = -2.2$ to -3.5) is of the same order as the one for RGPS data ($n \approx -3.1$). The PDF of the 4.5 km solution always shows the shallowest slope, followed by the 9 km one. The 18 km solution has the steepest slope. We do not observe the strong divergence from power-law scaling for the VP sea-ice rheology reported by Girard et al. (2009), neither for the spatial-scale dependence nor for the PDFs.

We tested if the power-law dependence can be used to compare deformation rates obtained with model simulations using different grid spacings. The scaling of the deformation rate in our three model solutions with different grid spacing, i.e., different length scales, follows a similar power law as is observed for the RGPS observations (Sect. 3.2.3). The power-law scaling exponent strongly depends on ice concentration and thickness, i.e., the factors that for the model determine the internal ice stress. In most cases, therefore, it will not be possible to meaningfully compare absolute numbers of strain rates obtained from models with different grid spacing.

The anisotropic filter presented in Bouillon and Rampal (2015a) improves all deformation fields and especially the ice divergence. The filter changes both the average values and magnitude of the power-law scaling exponents (Sect. 2.4). Qualitatively, however, the conclusions drawn from a comparison of the RGPS data with model simulations are the same for the filtered and unfiltered datasets.

On larger scales the sea-ice deformation rate of all three model solutions is very similar, with only small improvements for the 4.5 km simulation (Fig. 5). Almost independent of grid spacing, the modeled sea-ice deformation is much lower than the RGPS observations ($\sim 40\%$). Nevertheless, the large-scale pattern of divergence (Fig. 2) and vorticity (Fig. 3), and to a lesser degree shear (Fig. 4), are reproduced by all model simulations. Even if the differences are small for the large-scale deformation patterns, the 4.5 km simulation, the one with the smallest horizontal grid spacing, always performs best out of the three solutions. This difference be-

comes more pronounced if small-scale deformation features are considered. The 4.5 km simulation is the only one that reproduces a reasonable number of LKFs in the Central Arctic, even on length scales ($2\times$ the grid spacing) where the lower-resolution models theoretically are capable of reproducing these features. We conclude that increasing the spatial model resolution can improve the sea-ice deformation representation for a viscous–plastic sea-ice rheology. However, big differences to the observed sea-ice deformation strain rates still remain.

A realistic representation of sea-ice deformation in models is important for accurate simulation of the sea-ice mass balance. Multiple equilibrium flow states (i.e., when ice growth equals ice export) can exist for the Arctic Basin, and their characteristics are influenced by sea-ice strength and ice rheology (Hibler III et al., 2006). Steele et al. (1997) show that the ice strength parameterization in a VP sea-ice model influences the sea-ice mass balance in the Arctic Ocean. Reducing the sea-ice strength in the model decreases the internal stress gradient and results in faster mean ice motion and thicker ice, which in turn strengthens and slows the ice. Steele et al. (1997) attribute this thickening to increased ice piling up in the weaker ice simulation.

An interesting future study would be to attempt to adjust sea-ice and ocean model parameters in order to reproduce the metrics discussed in this paper. For example, in a separate sensitivity experiment, not discussed in this manuscript, we changed the sea-ice strength dependence on sea-ice thickness (Eq. 6) from linear to cubic, which considerably increased deformation rate in both perennial and seasonal ice zones. Of course, adjusting a single parameter can improve a certain set of model features but is likely to make others, e.g., sea-ice velocity, worse. What is needed is the simultaneous adjustment of several key model parameters, in the manner discussed in Menemenlis et al. (2005) and Nguyen et al. (2011). Other possible approaches for improving the representation of sea-ice strain rates include the introduction of multiple categories for different ice thicknesses and deformed and undeformed ice, since multi-category models allow weaker resistance, more leads, and enhanced ice growth (Mårtensson et al., 2012); and experimentation with new ice rheologies that do not rely on the viscous–plastic assumptions (Sulsky et al., 2007; Girard et al., 2011; Tsamados et al., 2013; Bouillon and Rampal, 2015b).

The Supplement related to this article is available online at https://doi.org/10.5194/tc-11-1553-2017-supplement.

References

Antonov, J. I., Locarnini, R. A., Boyer, T. P., Mishonov, A. V., and Garcia, H. E.: World Ocean Atlas 2005, Volume 2: Salinity, edited by: Levitus, S., NOAA Atlas NESDIS 62, U.S. Government Printing Office, Washington, D.C., 182 pp., 2006.

Barry, R. G., Serreze, M. C., Maslanik, J. A., and Preller, R. H.: The Arctic Sea Ice-Climate System: Observations and modeling, Rev. Geophys., 31, 397–422, https://doi.org/10.1029/93RG01998, 1993.

Bouillon, S. and Rampal, P.: On producing sea ice deformation data sets from SAR-derived sea ice motion, The Cryosphere, 9, 663–673, https://doi.org/10.5194/tc-9-663-2015, 2015a.

Bouillon, S. and Rampal, P.: Presentation of the dynamical core of neXtSIM, a new sea ice model, Ocean Model., 91, 23–37, https://doi.org/10.1016/j.ocemod.2015.04.005, 2015b.

Comiso, J. C.: Large Decadal Decline of the Arctic Multiyear Ice Cover, J. Climate, 25, 1176–1193, https://doi.org/10.1175/JCLI-D-11-00113.1, 2012.

Comiso, J. C., Parkinson, C. L., Gersten, R., and Stock, L.: Accelerated decline in the Arctic sea ice cover, Geophys. Res. Lett., 35, L01703, https://doi.org/10.1029/2007GL031972, 2008.

Coon, M., Kwok, R., Levy, G., Pruis, M., Schreyer, H., and Sulsky, D.: Arctic Ice Dynamics Joint Experiment (AIDJEX) assumptions revisited and found inadequate, J. Geophys. Res., 112, C11S90, https://doi.org/10.1029/2005JC003393, 2007.

Fenty, I., Menemenlis, D., and Zhang, H.: Global coupled sea ice-ocean state estimation, Clim. Dyn., 1–26, https://doi.org/10.1007/s00382-015-2796-6, 2015.

Girard, L., Weiss, J., Molines, J. M., Barnier, B., and Bouillon, S.: Evaluation of high-resolution sea ice models on the basis of statistical and scaling properties of Arctic sea ice drift and deformation, J. Geophys. Res., 114, C08015, https://doi.org/10.1029/2008JC005182, 2009.

Girard, L., Bouillon, S., Weiss, J., Amitrano, D., Fichefet, T., and Legat, V.: A new modelling framework for sea ice mechanics based on elasto-brittle rheology, Ann. Glaciol., 52, 123–132, 2011.

Heil, P. and Hibler, W. D.: Modeling the High-Frequency Component of Arctic Sea Ice Drift and Deformation, J. Phys. Oceanogr., 32, 3039–3057, https://doi.org/10.1175/1520-0485(2002)032<3039:MTHFCO>2.0.CO;2, 2002.

Hibler III, W. D., Hutchings, J., and Ip, C.: Sea-ice arching and multiple flow states of Arctic pack ice, Ann. Glaciol., 44, 339–344, 2006.

Hibler III, W. D.: A Dynamic Thermodynamic Sea Ice Model, J. Phys. Oceanogr., 9, 815–846, https://doi.org/10.1175/1520-0485(1979)009<0815:ADTSIM>2.0.CO;2, 1979.

Hibler III, W. D.: Modeling a Variable Thickness Sea Ice Cover, Mon. Weather Rev., 108, 1943–1973, https://doi.org/10.1175/1520-0493(1980)108<1943:MAVTSI>2.0.CO;2, 1980.

Hunke, E. and Dukowicz, J.: An elastic-viscous-plastic model for sea ice dynamics, J. Phys. Oceanogr., 27, 1849–1867, 1997.

Jakobsson, M., Macnab, R., Mayer, L., Anderson, R., Edwards, M., Hatzky, J., Schenke, H. W., and Johnson, P.: An improved bathymetric portrayal of the Arctic Ocean: Implications for ocean modeling and geological, geophysical and oceanographic analyses, Geophys. Res. Lett., 35, L07602, https://doi.org/10.1029/2008GL033520, 2008.

Kwok, R.: The RADARSAT Geophysical Processor System, in: Analysis of SAR Data of the Polar Oceans: Recent Advances, edited by: Tsatsoulis, C. and Kwok, R., Springer-Verlag, New York, 235–257, 1998.

Kwok, R. and Cunningham, G. F.: Seasonal ice area and volume production of the Arctic Ocean: November 1996 through April 1997, J. Geophys. Res., 107, 8038, https://doi.org/10.1029/2000JC000469, 2002.

Kwok, R. and Rothrock, D. A.: Decline in Arctic sea ice thickness from submarine and ICESat records: 1958–2008, Geophys. Res. Lett., 36, L15501, https://doi.org/10.1029/2009GL039035, 2009.

Kwok, R., Cunningham, G. F., and Pang, S. S.: Fram Strait sea ice outflow, J. Geophys. Res., 109, C01009, https://doi.org/10.1029/2003JC001785, 2004.

Kwok, R., Hunke, E. C., Maslowski, W., Menemenlis, D., and Zhang, J.: Variability of sea ice simulations assessed with RGPS kinematics, J. Geophys. Res., 113, C11012, https://doi.org/10.1029/2008JC004783, 2008.

Large, W., McWilliams, J., and Doney, S.: Oceanic vertical mixing: a review and a model with a nonlocal boundary layer parameterization, Rev. Geophys., 32, 363–403, 1994.

Lindsay, R. W. and Stern, H. L.: The RADARSAT Geophysical Processor System: Quality of Sea Ice Trajectory and Deformation Estimates, J. Atmos. Oceanic Tech., 20, 1333–1347, https://doi.org/10.1175/1520-0426(2003)020<1333:TRGPSQ>2.0.CO;2, 2003.

Lindsay, R. W., Zhang, J., and Rothrock, D. A.: Sea-Ice Deformation Rates from Satellite Measurements and in a Model, Atmos. Ocean, 41, 35–47, https://doi.org/10.3137/ao.410103, 2003.

Lindsay, R. W., Zhang, J., Schweiger, A. J., Steele, M. A., and Stern, H.: Arctic sea ice retreat in 2007 follows thinning trend, J. Climate, 22, 165–176, https://doi.org/10.1175/2008JCLI2521.1, 2009.

Lipscomb, W. H., Hunke, E. C., Maslowski, W., and Jakacki, J.: Ridging, strength, and stability in high-resolution sea ice models, J. Geophys. Res., 112, C03S91, https://doi.org/10.1029/2005JC003355, 2007.

Locarnini, R. A., Mishonov, A. V., Antonov, J. I., Boyer, T. P., and Garcia, H. E.: World Ocean Atlas 2005, Volume 1: Temperature, edited by: Levitus, S., NOAA Atlas NESDIS 61, U.S. Government Printing Office, Washington, D.C., 182 pp., 2006.

Losch, M., Menemenlis, D., Campin, J.-M., Heimbach, P., and Hill, C.: On the formulation of sea-ice models. Part 1: Effects of different solver implementations and parameterizations, Ocean Model., 33, 129–144, https://doi.org/10.1016/j.ocemod.2009.12.008, 2010.

Marcq, S. and Weiss, J.: Influence of sea ice lead-width distribution on turbulent heat transfer between the ocean and the atmosphere, The Cryosphere, 6, 143–156, https://doi.org/10.5194/tc-6-143-2012, 2012.

Marsan, D., Stern, H., Lindsay, R., and Weiss, J.: Scale dependence and localization of the deformation of Arctic sea ice, Phys. Rev. Lett., 93, 178501, https://doi.org/10.1103/PhysRevLett.93.178501, 2004.

Mårtensson, S., Meier, H. E. M., Pemberton, P., and Haapala, J.: Ridged sea ice characteristics in the Arctic from a coupled multicategory sea ice model, J. Geophys. Res., 117, C00D15, https://doi.org/10.1029/2010JC006936, 2012.

McPhee, M. G., Kwok, R., Robins, R., and Coon, M.: Upwelling of Arctic pycnocline associated with shear motion of sea ice, Geophys. Res. Lett., 32, L10616, https://doi.org/10.1029/2004GL021819, 2005.

Menemenlis, D., Fukumori, I., and Lee, T.: Using Green's Functions to Calibrate an Ocean General Circulation Model, Mon. Weather Rev., 133, 1224–1240, https://doi.org/10.1175/MWR2912.1, 2005.

Menemenlis, D., Campin, J., Heimbach, P., Hill, C., Lee, T., Nguyen, A., Schodlock, M., and Zhang, H.: ECCO2: High Resolution Global Ocean and Sea Ice Data Synthesis, Mercator Ocean Quarterly Newsletter, 31, 13–21, 2008.

Miller, P. A., Laxon, S. W., and Feltham, D. L.: Improving the spatial distribution of modeled Arctic sea ice thickness, Geophys. Res. Lett., 32, L18503, https://doi.org/10.1029/2005GL023622, 2005.

Nghiem, S. V., Rigor, I. G., Perovich, D. K., Clemente-Colón, P., Weatherly, J. W., and Neumann, G.: Rapid reduction of Arctic perennial sea ice, Geophys. Res. Lett., 34, L19504, https://doi.org/10.1029/2007GL031138, 2007.

Nguyen, A. T., Menemenlis, D., and Kwok, R.: Improved modeling of the Arctic halocline with a subgrid-scale brine rejection parameterization, J. Geophys. Res., 114, C11014, https://doi.org/10.1029/2008JC005121, 2009.

Nguyen, A. T., Menemenlis, D., and Kwok, R.: Arctic ice-ocean simulation with optimized model parameters: Approach and assessment, J. Geophys. Res., 116, C04025, https://doi.org/10.1029/2010JC006573, 2011.

Nguyen, A. T., Kwok, R., and Menemenlis, D.: Source and Pathway of the Western Arctic Upper Halocline in a Data-Constrained Coupled Ocean and Sea Ice Model, J. Phys. Oceanogr., 42, 802–823, https://doi.org/10.1175/JPO-D-11-040.1, 2012.

Onogi, K., Tsutsui, J., Koide, H., Sakamoto, M., Kobayashi, S., Hatsushika, H., Matsumoto, T., Yamazaki, N., Kamahori, H., Taka-hashi, K., Kadokura, S., Wada, K., Kato, K., Oyama, R., Ose, T., Mannoji, N., and Taira, R.: The JRA-25 Reanalysis, J. Meteorol. Soc. Jpn., 85, 369–432, 2007.

Rampal, P., Weiss, J., Marsan, D., and Bourgoin, M.: Arctic sea ice velocity field: General circulation and turbulent-like fluctuations, J. Geophys. Res., 114, C10014, https://doi.org/10.1029/2008JC005227, 2009.

Raney, R., Luscombe, A., Langham, E., and Ahmed, S.: RADARSAT [SAR imaging], Proceedings of the IEEE, 79, 839–849, https://doi.org/10.1109/5.90162, 1991.

Rignot, E., Fenty, I., Menemenlis, D., and Xu, Y.: Spreading of warm ocean waters around Greenland as a possible cause for glacier acceleration, Ann. Glaciol., 53, 257–266, https://doi.org/10.3189/2012AoG60A136, 2012.

Rothrock, D. A.: The Energetics of the Plastic Deformation of Pack Ice by Ridging, J. Geophys. Res., 80, 4514–4519, 1975.

Steele, M., Zhang, J., Rothrock, D., and Stern, H.: The force balance of sea ice in a numerical model of the Arctic Ocean, J. Geophys. Res., 102, 21061–21079, https://doi.org/10.1029/97JC01454, 1997.

Stern, H. L. and Lindsay, R. W.: Spatial scaling of Arctic sea ice deformation, J. Geophys. Res., 114, C10017, https://doi.org/10.1029/2009JC005380, 2009.

Sulsky, D., Schreyer, H., Peterson, K., Kwok, R., and Coon, M.: Using the material-point method to model sea ice dynamics, J. Geophys. Res., 112, C02S90, https://doi.org/10.1029/2005JC003329, 2007.

Tsamados, M., Feltham, D. L., and Wilchinsky, A. V.: Impact of a new anisotropic rheology on simulations of Arctic sea ice, J. Geophys. Res.-Oceans, 118, 91–107, https://doi.org/10.1029/2012JC007990, 2013.

Wang, K. and Wang, C.: Modeling linear kinematic features in pack ice, J. Geophys. Res., 114, C12011, https://doi.org/10.1029/2008JC005217, 2009.

Weiss, J.: Scaling of fracture and faulting of ice on Earth, Surv. Geophys., 24, 185–227, 2003.

Weiss, J.: Drift, Deformation, and Fracture of Sea Ice – A Perspective Across Scales, SpringerBriefs in Earth Sciences, Springer Netherlands, https://doi.org/10.1007/978-94-007-6202-2, 2013.

Zhang, J. and Hibler III, W. D.: On an efficient numerical method for modeling sea ice dynamics, J. Geophys. Res., 102, 8691–8702, https://doi.org/10.1029/96JC03744, 1997.

Zhang, J. and Rothrock, D. A.: Modeling Global Sea Ice with a Thickness and Enthalpy Distribution Model in Generalized Curvilinear Coordinates, Mon. Weather Rev., 131, 845–861, https://doi.org/10.1175/1520-0493(2003)131<0845:MGSIWA>2.0.CO;2, 2003.

Zhang, J., Hibler, W. D., Steele, M., and Rothrock, D. A.: Arctic ice-ocean modeling with and without climate restoring, J. Phys. Oceanogr., 28, 191–217, 1998.

Zhang, J., Thomas, D. R., Rothrock, D. A., Lindsay, R. W., Yu, Y., and Kwok, R.: Assimilation of ice motion observations and comparisons with submarine ice thickness data, J. Geophys. Res., 108, 3170, https://doi.org/10.1029/2001JC001041, 2003.

Zhang, J., Lindsay, R., Steele, M., and Schweiger, A.: What drove the dramatic retreat of arctic sea ice during summer 2007?, Geophys. Res. Lett., 35, L11505, https://doi.org/10.1029/2008GL034005, 2008.